

University of Windsor

Scholarship at UWindor

Electronic Theses and Dissertations

Theses, Dissertations, and Major Papers

4-14-2017

Effects of Heat Transfer on Vehicle Front-end Cooling Airflow Simulation

Stefan Tojcic
University of Windsor

Follow this and additional works at: <https://scholar.uwindsor.ca/etd>

Recommended Citation

Tojcic, Stefan, "Effects of Heat Transfer on Vehicle Front-end Cooling Airflow Simulation" (2017).
Electronic Theses and Dissertations. 5954.
<https://scholar.uwindsor.ca/etd/5954>

This online database contains the full-text of PhD dissertations and Masters' theses of University of Windsor students from 1954 forward. These documents are made available for personal study and research purposes only, in accordance with the Canadian Copyright Act and the Creative Commons license—CC BY-NC-ND (Attribution, Non-Commercial, No Derivative Works). Under this license, works must always be attributed to the copyright holder (original author), cannot be used for any commercial purposes, and may not be altered. Any other use would require the permission of the copyright holder. Students may inquire about withdrawing their dissertation and/or thesis from this database. For additional inquiries, please contact the repository administrator via email (scholarship@uwindsor.ca) or by telephone at 519-253-3000ext. 3208.

**EFFECTS OF HEAT TRANSFER ON VEHICLE FRONT-END
COOLING AIRFLOW SIMULATION**

By

Stefan Tojic

A Thesis

Submitted to the Faculty of Graduate Studies
through the Department of Mechanical, Automotive and Materials Engineering
in Partial Fulfillment of the Requirements for
the Degree of Master of Applied Science at the
University of Windsor

Windsor, Ontario, Canada

2017

© 2017 Stefan Tojic

**EFFECTS OF HEAT TRANSFER ON VEHICLE FRONT-END
COOLING AIRFLOW SIMULATION**

By

Stefan Tojcic

APPROVED BY:

Dr. G. Rankin, Program Reader

Department of Mechanical, Automotive and Materials Engineering

Dr. R. M. Barron, Outside Program Reader

Department of Mathematics and Statistics, Department of Mechanical, Automotive and
Materials Engineering

Dr. J. Johrendt, Advisor

Department of Mechanical, Automotive and Materials Engineering

23 January 2017

DECLARATION OF ORIGINALITY

I hereby declare that this thesis incorporates material, which is an outcome of a joint venture undertaken in collaboration with FCA Canada and the University of Windsor's Department of Mechanical, Automotive and Materials Engineering, under the supervision of Dr. J. Johrendt.

I hereby certify that I am the sole author of this thesis and that no part of this thesis has been published or submitted for publication.

I certify that, to the best of my knowledge, my thesis does not infringe upon anyone's copyright nor violate any proprietary rights and that any ideas, techniques, quotations, or any other material from the work of other people included in my thesis, published or otherwise, are fully acknowledged in accordance with the standard referencing practices.

I declare that this is a true copy of my thesis, including any final revisions, as approved by my thesis committee and the Graduate Studies office, and that this thesis has not been submitted for a higher degree to any other University or Institution.

ABSTRACT

This research focuses on virtual simulation techniques for vehicle underhood airflow. The main objective is to gain a better understanding of heat transfer effects on vehicle underhood cooling airflow and provide correction methods to increase the accuracy of simulations early in the vehicle development phase.

Simulations are carried out for a stand-alone radiator setup, based on three different flow assumptions; constant density iso-thermal, constant density with heat transfer, and variable density with heat transfer. It was observed that, in some cases, corrected heat exchanger porous resistance terms need to be adopted for each simulation case in order to provide good correlation with test data.

Similar flow assumptions are carried over to a full vehicle underhood simulation, for which additional components, such as a transmission oil cooler, condenser, and fan were modeled. It was observed that mass flow rates at the radiator inlet are over-estimated with the assumption of an incompressible iso-thermal flow; by 2% with respect to the incompressible simulation with temperature effects, and by 10% with respect to the variable density simulation with temperature effects. It is suggested that in order to capture the local increase in velocity field at the heat exchangers, it is necessary to perform simulations with a variable density. However, to establish confidence in the quantitative results, further studies regarding the impact of fan modelling and variable density effects should be performed.

DEDICATION

To my parents

For their love and support

And to whom I owe everything

ACKNOWLEDGEMENTS

The author is incredibly grateful to his academic and industrial advisors for the support throughout the entirety of this project; Dr. J. Johrendt, Dr. K. Srinivasan, Mr. S. Surapaneni, and Mr. E. Ribaldone. Additional thanks to Mr. M. Raza for his genuine interest and guidance.

I sincerely acknowledge the members of my committee, Dr. G. Rankin, Dr. R. M. Barron, and Dr. J. Johrendt, for their valuable time and feedback. I would also like to thank FCA Canada/University of Windsor Automotive Research and Development Centre (ARDC) as well as Centro Ricerche Fiat (CRF) for graciously extending the use of their computing facilities. In addition, a special thanks to Mr. M. Malik at ARDC for his assistance along the way, Dr. M. O. Iqbal for his help during the early part of this thesis, and Dr. E. Farbar for her invaluable support and patience towards the end of this research.

Finally, I am grateful to all family members and friends for their encouragement, support and patience during my graduate studies.

TABLE OF CONTENTS

Declaration of Originality	iii
Abstract	iv
Dedication	v
Acknowledgements.....	vi
List of Figures	ix
List of Tables.....	xii
Nomenclature	xiv
1. INTRODUCTION	1
1.1 Background	1
1.2 Motivation	2
1.3 Scope of Study	3
2. LITERATURE REVIEW	5
2.1 Introduction to Vehicle Thermal Management	5
2.2 Virtual Modelling.....	6
2.3 Fan Modelling	10
2.4 Heat Exchanger Analysis	13
2.5 Summary	13
3. NUMERICAL MODELLING	16
3.1 Introduction	16
3.2 Finite Volume Discretization	17
3.3 Governing Equations.....	18
3.3.1 Conservation of Mass	18
3.3.2 Conservation of Momentum	18
3.3.1 Turbulence Model.....	20
3.3.2 Conservation of Energy	22
3.4 Segregated Flow and Energy Model	24

3.5 Porous Media Formulation.....	25
3.6 Heat Exchanger Formulation	26
4. ISOLATED RADIATOR MODELLING.....	30
4.1 Introduction.....	30
4.2 Experimental Measurements.....	31
4.3 Virtual Simulation.....	36
4.4 Results and Discussion.....	40
5. FULL VEHICLE MODELLING	54
5.1 Introduction.....	54
5.2 Experimental Measurements.....	56
5.3 Virtual Simulation.....	60
5.4 Results and Discussion.....	70
6. CONCLUSIONS	81
7. RECOMMENDATIONS FOR FUTURE WORK	83
References	87
Appendix A – Standard Velocity Corrections	91
Appendix B – TOC and Condenser Data	92
Appendix C – Isolated Radiator Test Results.....	95
Vita Auctoris	98

LIST OF FIGURES

Figure 1.1: Historical and forecasted CO ₂ emissions by country/region, from [1]	1
Figure 1.2: Illustration of airflow in vehicle underhood compartment [2]	2
Figure 2.1: Pressure trace in typical vehicle underhood configuration [7]	6
Figure 3.1: Example of turbulent airflow aft of a sphere (http://www.qsstudy.com)	20
Figure 3.2: Time-averaged plot of the mean and fluctuating velocity components	20
Figure 3.3: Typical pressure drop-airflow velocity curve for heat exchanger	25
Figure 3.4: Topology of a dual-stream heat exchanger	27
Figure 4.1: Heat exchanger dimensions	31
Figure 4.2: Photo of tested heat exchanger	31
Figure 4.3: Simplified diagram of calorimeter test	31
Figure 4.4: Pressure drop-velocity curve, iso-thermal conditions	33
Figure 4.5: Pressure drop-velocity curves from experimental testing	35
Figure 4.6: Test room geometry	36
Figure 4.7: Full plane view of volume mesh	37
Figure 4.8: Mesh refinement around radiator core region	37

Figure 4.9: Coolant tanks and direction of water flow in radiator core	38
Figure 4.10: Correlation for pressure drop for <i>Case 1</i> iso-thermal conditions	40
Figure 4.11: Loss coefficients as a function of area contraction ratio for different Reynolds numbers, from Kays and London 1984 [38]	42
Figure 4.12: Vector plot illustrating inlet edge losses around radiator frame	44
Figure 4.13: Summary of total inlet and outlet losses in isolated radiator experiment.....	45
Figure 4.14: Heat transfer and flow friction characteristics for a sample of louvered fin compact heat exchangers, from Kays and London (1984) [38]	49
Figure 4.15: Correlation for pressure drop for <i>Case 2</i> ; incompressible with heat transfer.....	50
Figure 4.16: Correlation for pressure drop for <i>Case 3</i> ; variable density with heat transfer.....	51
Figure 4.17: Pressure drop-velocity curves for all isolated radiator simulations; <i>Case 1,2,3</i> with porous media coefficients (P_i , P_v)	53
Figure 5.1: Simplified schematic of climatic wind tunnel test	56
Figure 5.2: Climatic wind tunnel testing area.....	57
Figure 5.3: Vehicle experimental road test - engine speed vs. time	57
Figure 5.4: a) Full vehicle geometry b) Underhood layout.....	61
Figure 5.5: Heat rejection as a function of heat exchanger mass flow rate for a) Condenser b) TOC	62

Figure 5.6: Pressure drop as a function of heat exchanger inlet velocity for a) Condenser b) TOC	63
Figure 5.7: Pressure drop as a function of heat exchanger inlet velocity – curve corrections for a) Condenser b) TOC.....	64
Figure 5.8: a) Fan and shroud geometry b) Fan domain.....	65
Figure 5.9: Vehicle in representative wind tunnel	66
Figure 5.10: Full vehicle and wind tunnel volume mesh in xz -plane	67
Figure 5.11: Vehicle underhood mesh refinement regions	67
Figure 5.12: Mass flux distribution at radiator inlet for each simulation	72
Figure 5.13: Mass flux distribution at TOC inlet for each simulation case	74
Figure 5.14: Mass flux distribution at condenser inlet for each simulation.....	75
Figure 5.15: Mass flux distribution in vehicle underhood.....	76
Figure 5.16: Mass flux distribution in vehicle underhood transverse plane	78


LIST OF TABLES

Table 3.1: Example table of heat exchanger mapping technique	28
Table 4.1: Experimental test data, iso-thermal conditions.....	32
Table 4.2: Experimental test data step 14, with heat transfer	34
Table 4.3: Isolated radiator simulation parameters for each case	38
Table 4.4: Correlation of radiator pressure drop.....	40
Table 4.5: Inlet and outlet pressure losses from simulation analysis.....	46
Table 4.6: Results of simulation Case 2, incompressible with heat transfer	47
Table 4.7: Simulation results compared to experimental testing for <i>Case 2</i> and <i>Case 3</i> from Table 4.3.....	50
Table 5.1: Averaged vehicle test data	58
Table 5.2: Inertial P_i and Viscous P_v porous media resistance coefficient terms for underhood heat exchangers in simulation	64
Table 5.3: Summary of refinement regions and mesh size allocations.....	68
Table 5.4: Volume mesh cell count	68
Table 5.5: Summary of vehicle simulation cases.....	69
Table 5.6: Full vehicle experimental testing and simulation results.....	70
Table 5.7: Relevant radiator results for each simulation case	73

Table 5.8: Relevant TOC results for each simulation case	75
Table 5.9: Relevant condenser results for each simulation case.....	75
Table 5.10: Heat rejection rates and temperatures for each heat exchanger	78

NOMENCLATURE

A	Control volume face area
C_μ	Constant in turbulent viscosity
D	Deformation tensor, equation (3.7)
D_h	Hydraulic diameter
E	Total energy
f	Fanning friction factor, equation (4.1)
\mathbf{f}_b	Body force terms (vector)
G	Mass flux of fluid
H_e	Total enthalpy
I	Identity matrix
k	Thermal conductivity (fluid property) equation (3.3), turbulent kinetic energy equation (3.9)
K_c	Loss coefficient due to contraction of flow area
K_e	Loss coefficient due to expansion of flow area
L	Characteristic length of heat exchanger
\mathbf{n}	Normal vector to surface element dA
p	Pressure
\mathbf{q}	Heat flux vector
q_H	Heat source terms, equation (3.3)
R	Ideal gas constant
S_ϕ	Source term of scalar property ϕ

S_u	User-defined heat sources equation (3.10)
T	Viscous stress tensor
T_c	Cold fluid inlet temperature, single-stream heat exchanger
T_{c_i}	Cold fluid inlet temperature, dual-stream heat exchanger
T_{h_i}	Hot fluid inlet temperature, dual-stream heat exchanger
T_{ref}	Reference heat exchanger temperature, single-stream heat exchanger
	Velocity vector
v_c	Cell velocity, single-stream heat exchanger
V_c	Cell volume, single-stream heat exchanger
V_i	Cell volume, dual-stream heat exchanger
ν_t	Turbulent viscosity
σ	Stress tensor equation (3.3)
σ_e, σ_i	Area expansion, contraction ratio
ρ_m	Average of inlet and outlet density
μ	Dynamic viscosity
Γ	Diffusion coefficient
ϕ	Scalar quantity in general transport equation (3.4)

1. INTRODUCTION

1.1 Background

Sustainable solutions and technologies have been at the forefront of research for many industrial fields in the past few years. For the automotive industry, the focus has largely been on reducing emissions and fuel consumption. Led by the United States, E.U., and Japanese regulatory institutions, the automotive industry has worked tirelessly over the past several years to develop and improve technologies in order to meet the ever-increasing emissions and fuel consumption standards. The development by manufacturers of cleaner technologies can be seen from Figure 1.1. This figure shows the historical and forecasted data in terms of CO₂ emissions emitted by passenger cars, for different countries/regions. The focus on fuel consumption, emissions, vehicle energy management and energy storage will continue to rise in the coming years.

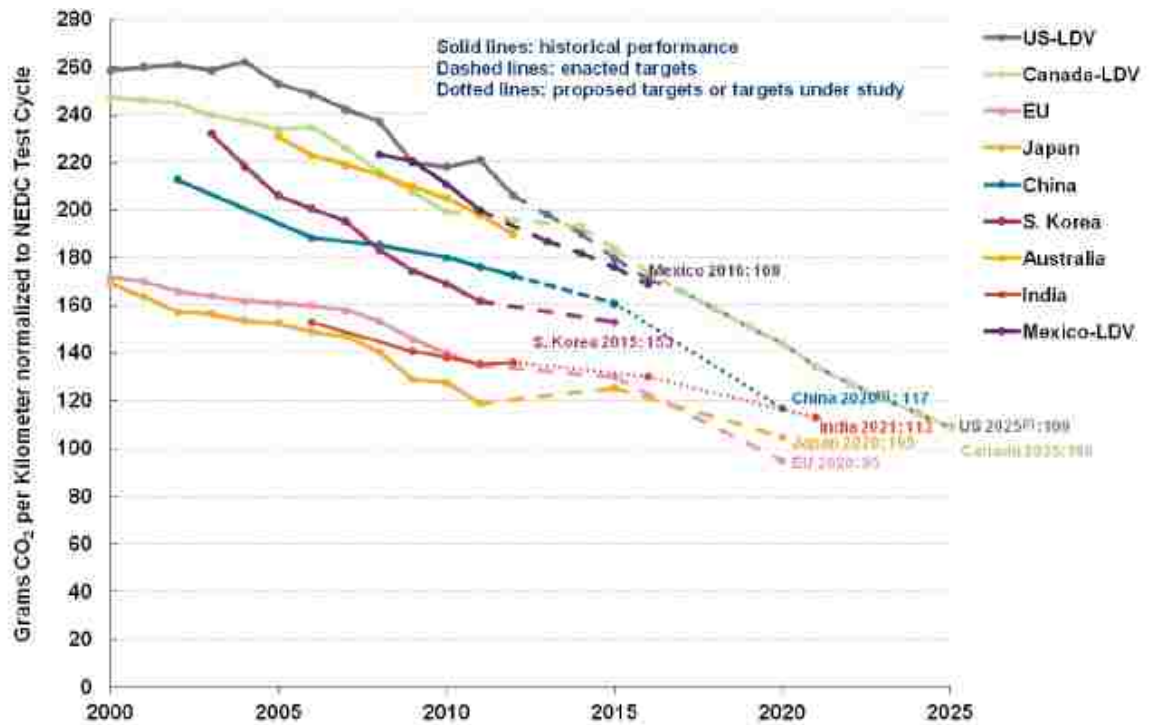


Figure 1.1: Historical and forecasted CO₂ emissions by country/region, from [1]

Significant changes have already been made to vehicles in order to achieve the emission and fuel consumption targets. For example, a common technology is engine turbocharging, resulting in engines that tend to run at higher relative temperatures and therefore require more heat rejection to operate at optimal efficiency. Another example would be aerodynamic improvements, which must also satisfy styling and customer appeal, and can directly affect cooling airflow. In addition, the last few years have seen various exhaust gas after-treatments introduced.

1.2 Motivation

Many of these adopted technologies have resulted in a much more complex underhood layout, while the general vehicle architecture has remained the same. This has resulted in additional constraints on the vehicle thermal management system.

With additional parts and components, there is less space for air to occupy and it becomes more difficult to evacuate this hot air and replace it. Combined with increased heat rejection required from today's engines, the issue becomes clear; less space and higher underhood temperatures. The demands of the thermal management system have therefore significantly increased and the system itself has become more complex, bringing with it additional components and packaging constraints as well.

Figure 1.2 shows a typical layout of an underhood compartment, with airflow inlet and outlet.

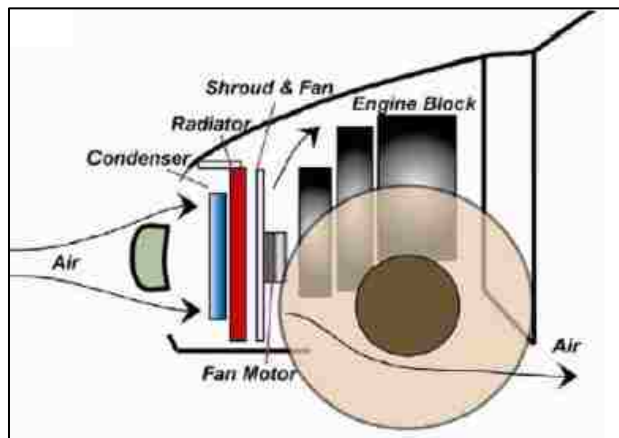


Figure 1.2: Illustration of airflow in vehicle underhood compartment [2]

The increasing complexity of the vehicle underhood compartment has led to an increased usage of virtual vehicle development. Projects become more expensive and complex due to the many components and subsystems involved in vehicle underhood development and analysis. In addition, projects are sure to include numerous departments and areas of specialization, and the need to cut costs and reduce lead times is becoming more important. This is where virtual development early in the vehicle development cycle is essential. Long before information is available on specific subsystems and before any prototypes are introduced, OEMs (Original Equipment Manufacturers) today need to have a prediction of the vehicle performance and capabilities. As these projects progress, changes downstream become inevitably more expensive, especially considering the already strict packaging constraints. In addition, any major re-designs may affect other subsystems and extend the project duration. This is the reason why virtual simulations have become a key focus for competitive OEMs.

Regarding thermal management, it is critical to have a good understanding of the complex underhood airflow process to be able to manage engine and overall temperatures more effectively. This goal is achieved with more detailed and accurate underhood airflow simulations.

1.3 Scope of Study

The focus of this thesis titled is to improve current 3D underhood simulations implemented early in the design cycle. More specifically, the goal is to gain a better understanding of the cooling airflow and its interaction with the various cooling modules when heat transfer effects are considered. The heat transfer effects are first investigated under the assumption of constant density flow. This assumption is then relaxed, to obtain a solution of the flow field that include the effects of variable density.

The commercial software tool STAR-CCM+ is used to perform the 3D CFD (Computational Fluid Dynamics) simulations, where the required inputs are provided by suppliers or in-house measurements. The results of the 3D simulations are validated using experimental data with an identical setup of geometry and conditions. 3D simulations are performed on an isolated radiator case and a full vehicle wind tunnel case, each discussed

in further detail in subsequent chapters. The full vehicle simulation will include the rest of the cooling modules in the example vehicle used for this thesis, such as a transmission oil cooler, condenser, radiator and single cooling fan. The modelling of each of these components will be discussed in further detail as well.

The current trend in industry is to use 1D and 3D simulations [3, 4] in combination to create an overall understanding of the vehicle thermal management system, as this provides further insight at both a system and component level. 3D simulations give the airflow characterization while it is possible to analyze system parameters with the 1D simulation. 1D simulations are outside the scope of this thesis and will be discussed only briefly, but are an essential part in the overall virtual model and can be used at different stages to increase accuracy and understanding of vehicle underhood thermal management.

2. LITERATURE REVIEW

2.1 Introduction to Vehicle Thermal Management

Automotive manufacturers have been challenged in recent years by more stringent regulations with regards to emissions and fuel consumption. Current standards agreed upon by automakers and regulators ensure nearly double the fuel efficiency and half the gas emissions for new vehicles by the year 2025 [1]. Other agreements include special credits for automakers using low-global-warming refrigerants and advanced technologies, such as plug-in electric vehicles, to achieve the target of 54.5 mpg (163 gCO₂/mile) by 2025 [5]. To deliver on the promise of more fuel efficient vehicles and better/less pollutants/emissions, automakers are developing new technologies and improving the performance of current technologies. This results in additional electrical and mechanical components in an already congested underhood compartment. The need to manage underhood temperatures has led to new challenges regarding the development of sophisticated cooling systems. Furthermore, vehicle underhood compartment studies involve both aspects of thermal analysis and aerodynamics. These phenomena are coupled and need to be taken into account to get an overall understanding of the complex airflow for the underhood compartment. Therefore, manufacturers must realize a balance between drag caused by the incoming airflow (known as cooling drag) and the required airflow for effective cooling [6]. The airflow entering the front vehicle constitutes a loss, and therefore needs to be used efficiently, to minimize this loss but maximize the cooling of the heat exchangers.

A typical pressure trace of the airflow entering the front of the vehicle and passing through the underhood compartment is shown in Figure 2.1. Depending on the need for cooling airflow under some vehicle operating conditions, the pressure restrictions shown in Figure 2.1 must be overcome. These restrictions consist of the general vehicle structure, component placement, and heat exchangers. The combination of ram air effect (air motion due to vehicle velocity) and fan is responsible for overcoming these pressure losses and providing adequate airflow for the cooling system.

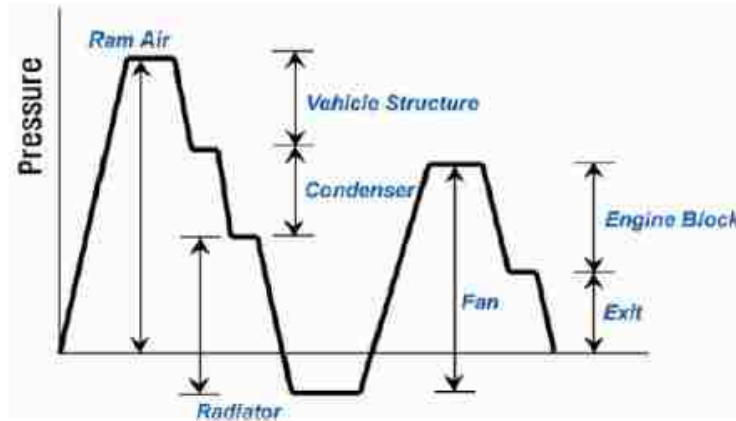


Figure 2.1: Pressure trace in typical vehicle underhood configuration [7]

2.2 Virtual Modelling

Typically in the past, vehicle thermal management system capabilities have been studied through experimental testing. With the advancement of numerical simulations and predictions, CFD has become a powerful tool in computing front-end airflow and estimating vehicle cooling packages early in the vehicle development cycle before any prototypes are developed. It is also possible to estimate a variety of design parameters, as evidenced by [2] and [8]. Regin et al. [2] use CFD to study the effect of different front-end opening area. With this evaluation, it was possible to estimate the cooling module requirements with the new design. The CFD results were validated with experimental wind tunnel testing, for which airflow was obtained with vane anemometers and various temperatures monitored with thermocouples. The results show that the CFD model can be used for the development of cooling modules for new vehicles and new designs. Singh and Shen [8] did a similar study of different parameters affecting cooling module performance and airflow using CFD software Fluent. Their methods were based on the principles of Taguchi's robust design methods to be applied early in a vehicle design phase. While this thesis will not evaluate any design changes for the front-end, it is evident that the capabilities of CFD software continue to expand and can save time and reduce cost when used at various stages of the vehicle development phase.

To capture the effects of the complete thermal management system, it is necessary to adopt numerical simulations which include 1D and 3D CFD approaches. Extensive

literature is available on this collaboration process, some of which is discussed in the next few pages. The reason for this is as follows; 3D simulations show the details of the flow as affected by structures and positions of different components, while 1D virtual modelling can capture the thermodynamic effects at a system level, such as heat rejection capabilities of the coolant loop [3, 4, 9].

Melzer et al. [10] proposed early concepts of vehicle thermal management with virtual modelling. While software capabilities at the time were limited, this soon changed, and new studies quickly followed. In [11, 12], a collaboration of multiple 1D softwares, such as FLOWMASTER, KULI, etc. are used to solve basic cooling problems. These models were further developed by the same authors. While 1D software and simulations were becoming a standard, early 3D CFD packages were being used to analyze the impact of underhood geometries and structures on the cooling modules [6]. This allowed further insight into the impact airflow distribution has on the cooling system process.

The next few pages provide more detail on some of the relevant research with regards to this thesis. While the focus in this thesis is 3D CFD modelling of the vehicle underhood compartment, it is shown that many of the approaches used are a combination of 1D, 3D and/or experimental testing.

Fortunato et al. [13] used a multi-step CFD approach to solve the thermal-flow field in the underhood compartment. Powerflow software, which is based on Lattice-Boltzmann (LB) methods, was used to solve for the velocity and pressure boundary conditions at the inlet and outlet of the underhood compartment. These boundary conditions were in turn used in STAR-CD, a Navier-Stokes solver, which performs the thermal analysis; both convective and radiation heat transfer was considered. All other components, including fan and heat exchangers, were modeled under the momentum source terms and porous media approach, respectively. The performance of these elements was obtained from characteristic curves. In addition, they considered a moving ground and rotating wheels as well, something that is not applied in this thesis, but which can influence the flow behaviour under the vehicle. The focus was on two operating conditions; low velocity climb and high speed. The simulations were compared with

experimental testing, for which information was obtained by thermocouples measuring some component surface temperatures and air temperatures. Results show the difference between simulated and measured temperatures to be within 10-15%.

An extension of the above work was performed by Alajbegovic et al. [14], where simulations to solve the full vehicle exterior and underhood region was performed also based on LB equations. The LB solver method is an alternative to the Navier-Stokes solvers, which is used in this thesis. The LB solvers are numerically efficient and robust, and can handle a large number of elements. There is also minimal work required for meshing, as only a surface mesher is required and the volume discretization requires minimal user input. The LB method has in past years gained considerable traction in industry, and the reader is referred to sources [15] and [16] for more detail on this method and its application.

This thesis is based on a Navier-Stokes solver coupled with heat exchanger calculations. Similar work was performed by [17, 18, 19], and will be discussed with other sources used to back up concepts and ideas.

Uhl et al. [20] performed CFD simulations of vehicle underhood and showed the interactive effects of heat exchangers, including charge air cooler (CAC), condenser, and radiator. The CFD software STAR-CD was used for the flow analysis, coupled with the in-house software BISS for the prediction of boundary conditions for the heat exchangers. Excellent insight into the validation of the simulations with experimental testing was provided, with 48 micro probes implemented to predict the velocity distribution of the radiator inlet face, in both cold and hot conditions (without and with a coolant flow). Quantitative information was given on the under/over-prediction of flow rate based on the micro probe measurements, which further illustrates the challenges of measuring air side parameters, also mentioned in [21]. Information regarding the influence of the fan on the measured parameters was also included, an important consideration, from both a testing and simulation perspective. Experimental measurements are further complicated when fan operation is included, while simplified models in the simulation for the fan do not capture the effects properly.

Furthermore, the point is stressed that any small geometrical details which alter the flow patterns and path can have a strong influence on the flow rate over the cooling module. This is also in-line with several other sources [17, 18, 22], which emphasize the need to accurately model the distance and gaps upstream and downstream of the cooling module. Even very small changes can influence cooling module behaviour. The complexity of this flow is further stressed with re-circulation issues. In [14], a numerical study of the underhood flow showed several regions of re-circulation that occur and interact with the heat exchangers. This provides further complexity to the airflow and prediction of heat exchanger behaviour. In order to minimize this re-circulation, especially at the radiator, several experiments were performed in order to determine which shielding methods could be applied. These shielding methods would provide more uniform velocity distribution at the radiator inlet, in order to increase cooling performance [19]. A similar procedure was undertaken in [23], where a CFD model in Fluent software was developed in order to understand the effects of air re-circulation in the radiator region.

Knaus et al. [24], used a coupled approach of 1D and 3D Navier-Stokes solvers to analyze various configurations of grille and front-end intake geometries for an example vehicle. Similar procedures for the heat exchanger and fan modelling were used as in [20] discussed above. Information is provided on the differences between two 3D softwares and fan modelling approaches adopted for each. An interesting note is the inability of the momentum source model applied to the fan to capture the re-circulation regions; this was applied to the software package UH3D. For the other 3D software, STAR-CD, the moving reference frame model for the fan required finer grid resolutions to predict the flow in the fan region, which greatly contributed to an increase in computational time. Mass flow predictions with simulation were found to be within 13% of experimental test data obtained with micro probes implemented in the radiator core.

Seider et al. [25] developed a prediction method for the automotive coolant network. The method is based on both 1D and 3D approaches, with boundary conditions exchanged between the 3D simulations in STAR and HPC, and 1D modelling in GT-COOL. Similar to previous methods already discussed, heat transfer and pressure maps for the heat exchangers were obtained from the component supplier, and were modeled as

porous blocks. The fan was modeled using a multiple reference frame approach at this stage, for which only the rotational speed was required as an input. Several vehicle operating conditions were modeled, most notably under an uphill driving conditions and high speed on a flat road. This approach is effective in analyzing the impact new powertrain components may have on the vehicle cooling performance and capabilities, before prototypes are available.

Despite the advancement in simulation tools, several sources still re-iterate the need for experimental testing in order to validate the simulations results, either with prototypes and/or real vehicles. In addition, numerical simulations often require boundary conditions to be extracted from experimental results, such as in [26, 27]. Several authors used experimental boundary conditions from experimental testing to focus on the interaction among different software tools [28, 29].

Wille et al. [30] developed an approach which uses numerical and experimental results to obtain the cooling air mass flow early in the vehicle development phase. 1D results, with all necessary input data included, were within 3% of CFD results, and provide fast turn-around times and the possibility to analyze transient behaviour, albeit in a limited degree of detail. 3D CFD offers the ability to analyze different configurations of a test bench, as well as the ability to analyze flow topology at any given position or component. Experimental testing of heat exchangers uses methods similar to previous sources, where the heat exchanger was fitted with pressure probes at the radiator. However, with 15 probes used over the surface of the heat exchanger, it was difficult to capture an accurate velocity distribution.

2.3 Fan Modelling

A common modelling approach observed in the sources discussed thus far is with regards to the fan modelling, which is generally modeled with a momentum source or moving reference frame (MRF) approach. Fan modelling has been, and is still today, a challenge to model accurately, especially with the full vehicle underhood geometry and physics. Capturing the fan effects is important because the fan is the main driver of

cooling airflow after the ram air effect. There are several methods available to model fans [31], the most common being:

1. Momentum Source Method/Body Force Method (BFM): This method is based on a steady state approach. The fan geometry is not present, but the fan momentum contribution is modeled with source terms in the transport equations. This method is relatively simple to implement and is not computationally expensive, but requires a map of the fan performance (a fan curve), typically obtained from stand-alone testing. In addition, this method does not take into account the swirl being produced by the fan. It is possible to include swirl via source terms, but these effects are commonly not measured.

2. Moving Reference Frame (MRF): This approach is the most common in industry, and uses the geometry of the fan. Using this method, the rotation of the fan is not explicitly modeled, but source terms for the momentum and turbulence are included in a rotating frame of reference equation. This is done for the control volume which makes up the fan, and is therefore a steady state simulation technique, a simplified modelling of the actual transient fan effects. The fluid region is separated into a rotating portion and a non-rotating portion, and a rotational speed is assigned to the volume of cells for which rotation exists i.e. between the blades. The major advantage with this method is that the only required input is the rotational speed of the fan, a parameter easily obtained without requiring further experimental testing.

3. Rigid Body Motion/Sliding Mesh (SM): In this model, the full detail of the fan geometry is included, and the momentum and turbulence are modelled with the actual rotation of the fan. This is sometimes referred to as a Sliding Mesh model because the interface between the rotating parts and non-rotating parts are allowed to slide against each other. This modelling technique is fully transient, and captures the full effects, as shown in [31]. However, it is very computationally demanding and is not feasible to apply in all cases, especially when considering estimation early in the vehicle development phase.

For this thesis, the fan modelling is not the main area of focus, but is recognized as one of the critical components which can affect the overall underhood model accuracy. The MRF model is applied in this thesis, for its low computational demand and because

no further testing of the stand-alone fan is required, as mentioned previously. In addition, there is substantial literature available with regards to MRF fan models applied to vehicle underhood CFD simulations. Most notably, the work by Gullberg et al. [31, 32, 33, 34, 35] has provided valuable insight with regards to fan modelling in general, and MRF modelling in particular. The work by Gullberg presented a correlation study which included an experimental test comprised of a typical underhood layout, with the measurement of the static pressure rise over the fan. Simulations were then performed with the MRF and SM approaches. The results showed that while the transient SM approach predicted the fan system quite well, the MRF significantly under-predicted the experimental results, more specifically, the pressure rise. This results in less air being drawn through the cooling package. This is also in-line with observations made by Wang et al. [36]. Both authors state that to be able to apply the MRF model accurately, the inlet and outlet interfaces of the fan region need to be placed where velocity and pressure are axisymmetric across the fan interface. This is nearly impossible in an underhood compartment.

With the stationary MRF approach, due to its simple application and low computational demand, Gullberg [34, 35] performed several additional studies to be able to apply the MRF model with as much accuracy as possible. Several studies followed, one of which outlined a correction method for the MRF approach. This correction approach is based on a 14% increase in the input speed for the simulation. This ensured relatively accurate predictions for cruising conditions, with some under-prediction still present at full fan engagement. There are still drawbacks to this method that need to be kept in mind, such as the further over-prediction of swirl (which will add more energy to the flow than what is available in reality), however it is a compromise, especially for early vehicle simulations. Additional studies were conducted on different fan geometries, and the reader is referred to the references mentioned above for more information on Gullberg's work with fan modelling.

2.4 Heat Exchanger Analysis

To gain a better understanding of heat exchanger modelling, including pressure drop correlations and heat transfer, the reader is referred to the excellent texts by Kakac and Liu [37], and Kays and London [38]. These texts provide valuable insight into heat exchanger design and modelling methods. Several equations and correlations in this thesis are adopted from these texts. In [37], the pressure drop and heat transfer equations are shown for several different heat exchangers. It is possible to use these equations in order to extract additional information regarding flow through the heat exchangers. As an example, it is possible to analyze the different effects of flow contraction and expansion on the heat exchanger pressure drop. Similar methods can be used to understand these effects in the experimental setup discussed in this thesis, and also for full vehicle situations. Data for several different types of heat exchangers, such as friction factor, Reynolds number, heat transfer coefficients, etc. is available, but mainly based on the pioneering work completed by Kays and London [38]. This text provides a comprehensive study of heat exchangers of various types and sizes, a valuable resource for nearly all studies involving heat exchangers. Quantitative information is used from this text to estimate the performance capabilities of the heat exchanger discussed in this thesis.

2.5 Summary

It has been shown that virtual vehicle modelling is an important tool in the prediction and development of the vehicle thermal management system. A combination of 1D and 3D tools can be used at different stages in the vehicle development process to reduce lead times and reduce cost associated with testing and prototypes. 1D, while able to obtain quick solutions, cannot capture the characteristics of the flow as in 3D. Virtual modelling is becoming more capable, but it is rarely the case that testing is not conducted at some stage, and is sometimes even a requirement to obtain boundary conditions for the simulation case.

Several techniques are used in testing to predict heat exchanger flow and thermal fields in order to validate the simulation techniques. Some tests are based on stand-alone

component test bench, while others attempt to replicate the upstream and downstream boundaries with simple structures. The most reliable technique seems to be the installation of micro probes in the heat exchanger core in order to measure the velocity/temperature distribution at the core. These probes have minimal impact on the core pressure drop. Other techniques, while available, produce high errors especially when conducted in a full vehicle wind tunnel environment.

Fan modelling options are limited for specific software packages, but usually depend on simplified models. These simplified models are generally used in order to capture some effect of the fan while maintaining a low computational demand, especially early in the vehicle development process. The most common approach is the Moving Reference Frame (MRF). Experimental measurements of fan effects are discussed in several sources of literature, many of which include no blockage effects upstream and downstream of the fan. The MRF model is known to be influenced by the presence of various components and non-symmetry, a situation unavoidable for a typical vehicle underhood compartment. Thus, applying these experimental techniques to validate the simulation data has proved difficult.

Heat exchangers are modeled using a porous media approach, since resolving the full geometry of a heat exchanger would be computationally expensive. Source terms are included in the governing equations in order to capture the pressure drop across the heat exchanger and any heat sources/sinks.

Full vehicle modelling is generally performed on a setup which requires upstream and downstream boundary conditions, as well as individual component temperatures in the underhood compartment. In another case, it is also possible to perform the simulations based on a half-vehicle or underhood layout only, however, additional boundary conditions need to be resolved beforehand. Modelling approaches using Lattice-Boltzmann methods or Navier-Stokes methods are common in vehicle underhood modelling. The software STAR-CCM+ used in this thesis is based on the Navier-Stokes approach. Typical meshing techniques used in the past include tetrahedral meshes, but more recently, hexahedral meshes have become available and can reduce pre-processing and simulation setup time. For more complex geometries and flow patterns, polyhedral

meshing can be used, although this results in more cells for a similar geometry and therefore an increase in computational demand.

Underhood simulations may be performed under iso-thermal constant density conditions, where the temperature field is not taken into account. This is appropriate in the case that predictions for heat rejection rate for the heat exchangers is not yet available, or the geometry for the underhood has not yet been resolved. Otherwise, most simulations consist of estimated heat sources for the heat exchangers based on 1D simulations or supplier data. The flow domain is still treated as constant density however. Limited literature is available on variable density effects for underhood simulations. This is a natural assumption to make, since Mach numbers are very low and therefore the airflow can be considered incompressible. However, since air density is a function of temperature, this thesis will explore the effects of variable density as well, through the use of the ideal gas law as the equation of state. It is possible also to use other methods which capture the density variations, such as look-up tables or polynomial functions.

Low vehicle and high fan speed operation representing a hill-climbing condition is regarded as the most severe operating condition for the cooling system performance. On the other hand, aerodynamic performance is typically evaluated at higher vehicle speeds on a flat road. In this thesis, the cooling system capabilities are of interest, and simulations are performed based on tested data from the hill-climbing condition.

Of particular interest is the mass flow rate (or mass flux) at the radiator inlet, in order to ensure adequate cooling capabilities under various engine operating conditions. Today's engines operate most efficiently in a specific range and require more complex heating and cooling phases. Therefore, it is important to accurately predict the airflow available at the radiator inlet. This is also true early in the vehicle development cycle, since a good prediction early in the program can reduce the need to make major changes later, which can become expensive. It is also beneficial to send required specifications or heat rejection rates to the suppliers early on, since lead times for such components tend to be high.

3. NUMERICAL MODELLING

3.1 Introduction

The most common method today to model fluid flow in three dimensions is derived from Continuum Mechanics where materials are modeled as a continuous mass rather than discrete particles, and is based on the fact that basic properties such as mass, momentum, and energy are conserved at all times. The laws governing fluid dynamics are commonly known as the Navier-Stokes equations, shown below; Conservation of Mass (3.1), Conservation of Momentum (3.2), and Conservation of Energy (3.3) (Kolditz, 2002) [39]:

$$\frac{\partial \rho}{\partial t} + \vec{\nabla} \cdot (\rho \vec{v}) \equiv 0$$

$$\rho \cdot \frac{\partial \vec{v}}{\partial t} + \rho (\vec{v} \cdot \vec{\nabla}) \vec{v} = - \vec{\nabla} p + \mu \left[\Delta \vec{v} + \frac{1}{3} \cdot \vec{\nabla} (\vec{\nabla} \cdot \vec{v}) \right] + \rho \vec{f}_e$$

$$\frac{\partial \rho E}{\partial t} + \vec{\nabla} \cdot (\rho \vec{v} E) = \vec{\nabla} \cdot (k \vec{\nabla} T) + \vec{\nabla} \cdot (\vec{\sigma} \cdot \vec{v}) + \rho \vec{f}_e \cdot \vec{v} + q_H$$

The above equations can be represented in multiple ways. Here they are shown as Partial Differential Equations (PDEs) in the general form. The fundamental concept of numerical schemes used in computational fluid dynamics (CFD) is based on the approximation of these PDEs by algebraic equations, which can then be solved numerically with a software tool.

In this section, a brief description of the numerical approach will be summarized along with solution techniques specific to the CFD commercial software tool STAR-CCM+ that is used. STAR-CCM+ is a CFD software which is able to perform complex three-dimensional calculations involving flow, heat transfer, and stress. It includes a wide range of capabilities in one software package; CAD modelling, surface preparation, advanced meshing capabilities, model solving and post-processing. It is also able to handle large models and allows parallel processing to optimize computational time. In addition, several analysis packages can be coupled with STAR-CCM+ to further enhance

the modelling and simulation, such as Abaqus, Radtherm, or ANSYS (Star-CCM+ User Manual v9.06) [40].

3.2 Finite Volume Discretization

To explain the transformation of the conservation equations (3.1) to (3.3) to a system of algebraic equations, a discretization method is required. A discretization method is simply the process of converting a partial differential equation into a form that is suitable for numerical solution. For CFD purposes, there are several discretization methods, such as Finite Difference Method (FDM), Finite Element Method (FEM), and the Finite Volume Method (FVM), [39].

STAR-CCM+ uses a finite volume method to discretize the integral form of the governing equations directly in physical space, which is made of a finite set of control volumes. The FVM has two major advantages in that it ensures conservation of quantities, such as mass, momentum, and energy at a local scale, therefore fluxes between control volumes are balanced. It is also possible to use FVM with structured or unstructured meshes.

The general transport equation (or conservation law) is the fundamental concept behind the conservation laws of mass, momentum and energy. It is shown here in integral form (Versteeg & Malalasekera, 2007) [41]:

$$\underbrace{\frac{\partial}{\partial t} \int_V \rho \Phi dV}_{\text{Transient Term}} + \underbrace{\oint_A (\rho \vec{v} \Phi) \vec{n} dA}_{\text{Convective Flux}} = \underbrace{\oint_A (\Gamma_\phi \nabla \Phi) \vec{n} dA}_{\text{Diffusive Flux}} + \underbrace{\int_V S_\phi dV}_{\text{Source Term}}$$

Where ϕ represents the transport of a scalar quantity. The four terms in the above equation represent:

- The transient term, which describes the variation per unit time of the quantity ϕ within the control volume V
- The convective flux term, which represents the amount of the property ϕ that is transported across the control volume boundaries (or through the surface) A , by the flow

- The diffusive flux term, which represents the amount of the property ϕ transported across the control volume boundaries (or through the surface) A , due to diffusion or molecular agitation
- The source term, which expresses the generation or destruction of the property ϕ inside the control volume V

These terms are further elaborated in the referenced text [41] and in the STAR-CCM+ User Manual [40].

3.3 Governing Equations

3.3.1 Conservation of Mass

The law of mass conservation expresses the fact that mass cannot be created nor destroyed in a fluid system. Applying this principle to a finite control volume,

$$\frac{\partial}{\partial t} \int_V \rho dV + \oint_S \rho \vec{v} \cdot \vec{n} dA = 0$$

Equation (3.5) is the general mass conservation equation in integral form. Note that there is no diffusion flux term for the mass transport, which means that mass is only transported across the boundaries through the convective term. Equation (3.5) is also commonly referred to as the continuity equation.

3.3.2 Conservation of Momentum

The equation for the conservation of linear momentum is based on the physical principle referred to as Newton's second law, $F=ma$. The forces experienced by a fluid element can be separated into external forces (body forces) and internal forces (surface forces). Surface forces include forces that act directly on the surface of the fluid element, such as the pressure force and stress due to the surrounding fluid elements. Body forces, sometimes referred to as volume forces, act directly on the mass of the fluid element, such as gravity.

The momentum equation applied to a control volume yields:

$$\frac{\partial}{\partial t} \int_V \rho \vec{v} dV + \oint_A (\rho \vec{v} \cdot \vec{n}) \vec{n} dA = - \oint_A p \mathbf{I} \vec{n} dA + \oint_A \mathbf{T} \vec{n} dA + \int_V (\sum f_i) dV$$

The terms on the left hand side of equation (3.6) are the transient term and the convective flux. The right hand side includes the pressure gradient term, the viscous flux where \mathbf{T} is the viscous stress tensor, and lastly the body force terms f_i . The body force terms may include effects of system rotation f_r , gravity f_g , porous media f_p , user-defined forces f_u , vorticity confinement f_w , or Laplace forces f_L .

Note here, the fluid is assumed to be a Newtonian fluid, for which the shear stress is related to the velocity field through a constant viscosity,

$$\mathbf{T} = 2\mu \mathbf{D} - \frac{2}{3} (\nabla \cdot \mathbf{v}) \mathbf{I}$$

where \mathbf{D} is the deformation tensor, μ is the constant dynamic viscosity, and \mathbf{I} is simply the unit tensor or identity matrix.

The equation for conservation of linear momentum is often referred to as the Navier-Stokes equation. However, in many cases in CFD literature, the term Navier-Stokes is used to include both linear momentum and continuity, and in some cases energy. Navier-Stokes equations refer to the governing equations that describe a particular flow as applied to a *viscous* fluid. In a constant density flow, the continuity and momentum equations can be solved to describe the fluid flow, without consideration of the temperature field or energy equation. STAR-CCM+ uses a specific model called the Segregated Flow model, which is discussed in a later section.

3.3.1 Turbulence Model

Most flows occurring in engineering are dominated by inertial forces rather than viscous forces, and are therefore associated with high Reynolds numbers. These flows are classified as turbulent, and should naturally be included in the current discussion. This section will provide a brief description on turbulence and the model used in this thesis.

One of the most important challenges in the field of CFD is the modelling and solving of turbulent flows. Turbulent flow is chaotic and random, as shown in Figure 3.1, where velocity and other flow properties vary constantly.

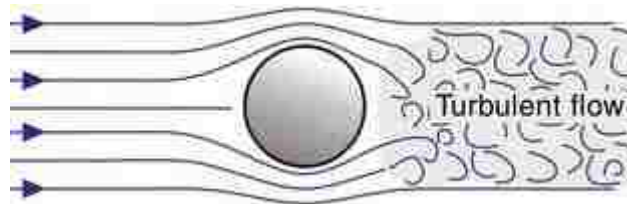


Figure 3.1: Example of turbulent airflow aft of a sphere (<http://www.qsstudy.com>)

The most accurate method to numerically solve the continuity and momentum equations for a turbulent flow is with Direct Numerical Solution (DNS) methods. This means solving the governing equations for the whole range of turbulence scales in the domain. The computational cost is high and therefore this method is not practical and not available even with the power of computers today for most industrial applications. Instead, it is more feasible to solve for averaged quantities of the flow properties while approximating the impact of the fluctuations. As an example, the velocity at some point in the flow may result in a plot as shown in Figure 3.2

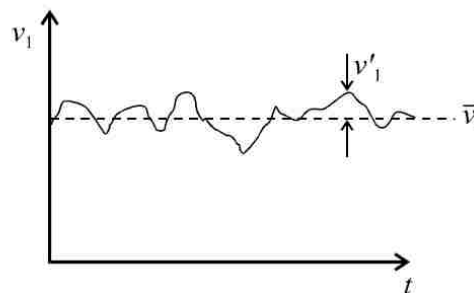


Figure 3.2: Time-averaged plot of the mean and fluctuating velocity components

The (transient) velocity is composed of a steady mean value \bar{v}_i (time-averaged) and a fluctuating component v_i' . Hence,

$$v_i(t) = \bar{v}_i(t) + v_i'(t)$$

In order to model the flow parameters in such a fashion, a time-averaged version of the continuity and momentum equations must be solved. These are termed the Reynolds-averaged Navier-Stokes equations (RANS), which are the basis for solving a variety of flow problems involving turbulence in today's CFD softwares.

The procedure of time-averaging comes at a cost – additional unknowns, namely Reynolds stresses, are introduced. Additional relationships between the unknown quantities are required and are solved with supplementary equations, known as turbulence models.

There are numerous turbulence models in use with a wide range of complexity, yet each is still an approximation to the phenomena of turbulence. Each model has its strengths and weakness and no 'best' model exists for all applications of flow. The effectiveness of a turbulence model is based purely on the type of flow to which it is applied.

The turbulence model used for this thesis project is a special form of the well-known k- ϵ model. k- ϵ models are classified as two equation models because they define the turbulent viscosity ν_t as a function of the turbulent kinetic energy k and the turbulent dissipation rate ϵ . Note that for the standard k- ϵ model, c_μ is a constant determined from experimental results.

$$\nu_t = c_\mu \frac{k^2}{\epsilon}$$

k- ϵ turbulent models have become an industry standard due to their robustness and application to many industrial flow problems. However, they show poor accuracy for some specific applications since the constant c_μ depends on the type of flow. Those flows, such as flows with separation and/or rotation, may result in significant errors with this

turbulence model. Therefore, many modifications of the standard k- ϵ model have been developed over the last years. The specific one used in these simulations is the realizable k- ϵ model [40], which provides superior accuracy over the standard model; the realizable k- ϵ model contains a new improved formulation for the turbulent viscosity and a new transport equation for the dissipation rate. For further definitions and development of this model, the reader is referred to the work done by Shih [42].

The k- ϵ models require a near-wall treatment to solve the boundary layer, which is one of the disadvantages and may increase computational time. The wall treatment used is the two-layer all- y^+ treatment, which is consistent with the two-layer turbulence model and produces reasonable approximations for meshes of a wide range of resolutions according to [40]. This has become a widely used model, and is adopted in this thesis as well. The effect of different turbulence models on the outcome of this research is not within the scope of this thesis.

3.3.2 Conservation of Energy

The conservation of energy equation stems from the first law of thermodynamics, which states that the change in total energy of a system is due to the rate of work on the system and heat transmitted to the system. This total energy is also defined as the sum of internal energy and kinetic energy per unit mass. The integral form of the energy equation is:

$$\frac{\partial}{\partial t} \int_V \rho E dV + \oint_{\Lambda} (\rho H_e \vec{v}) \cdot \vec{n} dA = - \oint_{\Lambda} \vec{q} \cdot \vec{n} dA + \oint_{\Lambda} (T \vec{v}) \cdot \vec{n} dA + \int_V \vec{f}_e \cdot \vec{v} dV + \int_V S_u dV$$

On the left hand side, E is the total energy, defined as the sum of the internal energy, kinetic energy, and gravitational potential energy. H_e is the total enthalpy, and it related to the total energy by,

$$E = H_e - \frac{p}{\rho}$$

In addition, a distinction has to be made between the different sources of the energy variation in the right hand side of the equation. It includes the heat flux vector q'' known as Fourier's law of heat conduction, the viscous stress tensor T , body forces f_e (such as gravity), and other heat sources s_u that are user-specified. Refer to the nomenclature for a full description of the above terms.

Up until this point, the governing equations for fluid flow have been presented in integral form, with a brief explanation of some of the terms contained in the equations. The end result is a system of five equations with six unknowns; ρ , p , u , v , w , E , excluding the additional turbulence terms k and ϵ that also need to be solved. In order to provide closure to the system of equations, an equation of state (or constitutive equation) is required to solve the unknowns. General equation of state models compute the density and density derivatives with respect to temperature and pressure. Different assumptions of the flow lead to different equations of state. As an example, in aerodynamics, it is generally accepted to assume a gas as a perfect gas, i.e. modeled using the ideal gas law,

$$P = \rho RT$$

This results in an additional equation, but also an additional unknown, leading to another seventh equation to close the system of equations, usually expressed with energy E as a function of two other thermodynamic variables, such as pressure p and temperature T ,

$$E = E(p, T)$$

The ideal gas law expresses density as a function of pressure and temperature, and therefore results in a coupled system of equations. On the other hand, by assuming an incompressible flow, the density is constant. This results in an uncoupling of the energy equation from the momentum and continuity equations with fewer unknowns.

3.4 Segregated Flow and Energy Model

To solve the velocity, pressure, and temperature fields, the Segregated Flow and Segregated Energy models are used in STAR-CCM+. They are summarized here.

The segregated flow model solves the discretized equations of continuity (3.14) and momentum (3.15) for the variables u , v , w , and p in a ‘segregated’ or sequential manner,

$$\sum (\dot{m}^*_f + \dot{m}'_f) = 0$$

$$\frac{\partial}{\partial t} (\rho v V)_0 + \sum [\rho v v \cdot a]_f = - \sum (p \mathbf{I} \cdot a)_f + \sum T \cdot a$$

The derivation of these equations is further discussed in [40].

This must be done iteratively in order to achieve a converged solution. This solver uses a pressure-velocity coupling algorithm, *SIMPLE*, which stands for Semi-Implicit Pressure Linked Equation. The steps are summarized below as per the STAR-CCM+ User Manual. In this algorithm, in order for the mass conservation law to be fulfilled for the velocity field, a pressure-corrector equation (known as a predictor-corrector approach) is derived from the conservation of mass equation and solved, where pressure as a variable is the obtained parameter.

Segregated Flow model steps:

1. Set boundary conditions
2. Compute velocity and pressure gradients
3. Solve discretized mass and momentum equations
4. Compute the uncorrected mass fluxes at the faces
5. Solve the pressure correction equation, which produces some pressure correction value
6. Update the pressure field, taking some under-relaxation pressure factor into account
7. Update the boundary condition pressures

8. Correct face mass fluxes
9. Correct the cell velocities
10. For compressible flow, update the density due to pressure changes
11. Free temporary storage and repeat

The Segregated Energy model supports the Segregated Flow models, and is available in three configurations. In this thesis, the Segregated Fluid Temperature energy model is used. This model solves the discrete energy equation (3.16), with temperature as the unknown variable.

$$\frac{\partial}{\partial t}(\rho E V_0) + \sum_f \left\{ \left[\rho H(v - v_s) + v_g p + \bar{q}'' - (T \cdot v) \right] \cdot a \right\}_f = (f \cdot v + s) V_0$$

The temperature is then solved according the equation of state chosen by the user. For further information regarding these solvers, the reader is referred to [40].

3.5 Porous Media Formulation

For the case of underhood flow simulations, a common method to model heat exchangers is to use a porous media model. This model incorporates a pressure drop that is a function of the fluid velocity in a cell. The flow resistance is usually measured from experimental setups, and a curve as shown in Figure 3.3 is obtained:

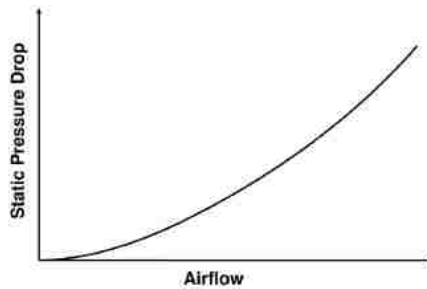


Figure 3.3: Typical pressure drop-airflow velocity curve for heat exchanger

The porous media model consists of a momentum source/sink term in the Navier-Stokes equations. This source term typically consists of a porous inertial term, P_i (quadratic) and a porous viscous term, P_v (linear), fitted to the curve shown above. Equation (3.18) is known as the Darcy-Forcheimer law and is the general representation of this source term,

$$P = - (P_v \mu \mathbf{v} + P_i \rho |\mathbf{v}| \mathbf{v})$$

The porous media model is used for each heat exchanger found in the example vehicle used in this thesis, including a TOC (transmission oil cooler), condenser and radiator. The porous terms obtained for each are highlighted in the 3D simulation section.

A major advantage of using a porous media model is that there is no need to model the exact geometry of the heat exchangers, which includes hundreds or thousands of tubes and fins, to extract information of interest. Instead, this is achieved with source terms which impose the known pressure drop across the heat exchanger. This also decreases the computational time considerably.

3.6 Heat Exchanger Formulation

Similar to adding momentum source terms for the porous media, energy source terms S_u in the energy equation (3.10) can be added to model heat transfer. To do this, a heat exchanger topology must exist.

Two different types of heat exchangers are used in this thesis. The first one is referred to as a single-stream heat exchanger, where only one of the fluid streams is explicitly modeled, while the second fluid is assumed to have a specified uniform temperature. The fluid of interest is modeled by activating a heat exchanger enthalpy source, which introduces a specified heat source or sink in the region of interest. With only one fluid being modeled, it is fairly simple to implement and requires minimal computational effort. Further insight into the computation of the local cell heat exchange value is provided by equation (3.19),

$$Q_c = Q_{total} \frac{V_c v_c (T_{ref} - T_c)}{\sum V_c v_c (T_{ref} - T_c)}$$

where Q_{total} is the user specified heat exchange, and T_{ref} is the constant temperature of the fluid stream that is not explicitly modeled.

The second type of heat exchanger is a dual-stream heat exchanger. In this case, both fluids are modeled, the hot and cold streams. With this type of heat exchanger, two identical overlapping regions with the same volume mesh are used to create a heat exchanger interface, as shown in Figure 3.4. Therefore, identical meshes are created in the same region.

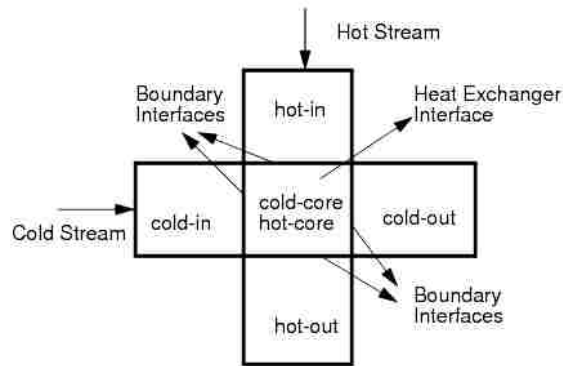


Figure 3.4: Topology of a dual-stream heat exchanger

Each fluid has its own respective region in which heat sources/sinks are introduced in the corresponding fluid energy equations. Both fluids are assumed to occur in single phase only (liquid or gas), and that no phase change occurs, as is typically seen with condensers in automotive vehicles. There are two types of dual-stream heat exchangers; basic and actual. The *actual dual-stream* model is used in this study, which will be the focus in subsequent discussion.

For this type of dual-stream heat exchanger, heat transfer behaviour must be provided by the user and STAR-CCM+ offers several options in this regard. In this study, a $Qmap$ table is used to model the heat exchanger performance for different flow rates of air and coolant, and is typically information obtained from experimental testing. This table is made of three columns; an example is shown below. It is used to calculate the local heat transfer coefficient UAL for each row.

Cold mass flow rate (kg/s)	Hot mass flow rate (kg/s)	Average heat rejection rate (W)
1.0	3.0	10,000
2.0	3.0	15,000
1.0	4.0	18,000
2.0	4.0	23,000

Table 3.1: Example table of heat exchanger mapping technique

The dual-stream heat exchanger approach calculates the local heat exchange Q_i using a local (cell) heat transfer coefficient ual_i ,

$$Q_i = \frac{ual_i(Th_i - Tc_i)V_i}{\left(\frac{1}{NC}\right)\sum_{i=1}^{NC} V_i}$$

Note that ual_i is obtained by considering the hot and cold mass fluxes entering cell i . Th_i and Tc_i are the local hot and cold stream temperatures entering cell i , while V_i is the cell volume.

UAL for the table is computed as,

$$UAL = \frac{\Gamma}{\Delta T_{net} \cdot NC}$$

where,

- NC is the total number of cells in the heat exchanger region
- ΔT_{net} is the volume averaged (cell ' i ' volume divided by the average cell volume) temperature difference between the hot and cold streams, calculated as

$$\Delta T_{net} = \frac{\sum_{i=1}^{NC} (T_{hi} - T_{ci})V_i}{\sum_{i=1}^{NC} V_i}$$

- Γ is calculated as,

$$\Gamma = Q \frac{(T_{hot,inlet} - T_{cold,inlet})}{(T_{hot,user} - T_{cold,user})}$$

where $T_{hot,user}$ and $T_{cold,user}$ are the temperature of the hot and cold stream respectively, as provided in the $Qmap$ table specifications and based on experimental measurements. Note that the above formula for Γ can be considered a scaling of the boundary temperatures; experimental testing can be performed with temperatures other than the required. There are two approaches that can be used to predict heat exchanger performance. In the first method, the hot stream inlet temperature is user-defined (*specified hot inlet*), and STAR-CCM+ will use this temperature with the $Qmap$ table to predict the heat rejection rate to the cold region. This is the method that is used in this study. In the other approach, the user can specify a heat rejection rate (*target heat rejection rate*), and the software will use this in accordance with the $Qmap$ table to back-calculate the required hot inlet temperature in order to sustain the specified heat rejection rate.

4. ISOLATED RADIATOR MODELLING

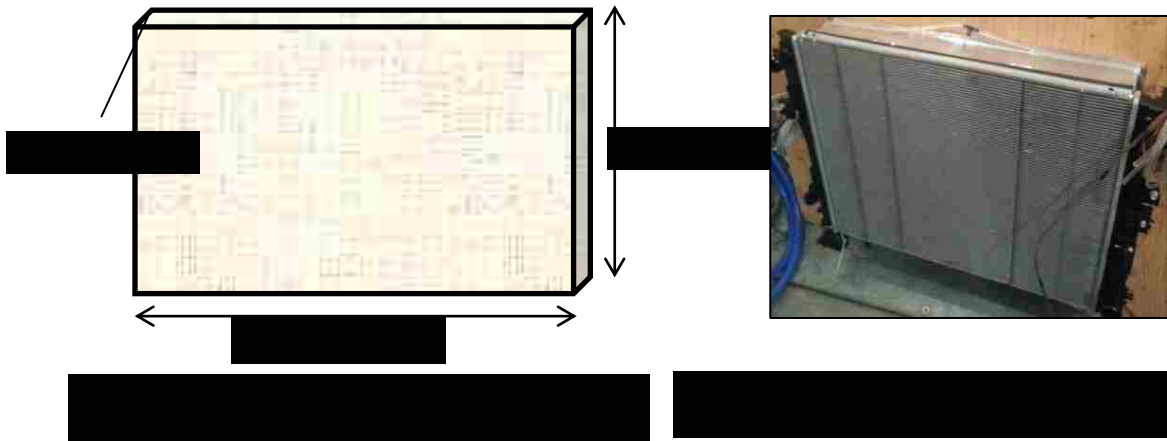
4.1 Introduction

The focus in this section is on the modelling of a stand-alone radiator. The basic task of a radiator is to cool down the hot coolant which extracts thermal energy from the engine and keep the engine operating at an optimal temperature. The radiator, in comparison to other underhood heat exchangers, has some of the highest heat rejection rates and largest surface area, making it a critical component in modelling and understanding of the underhood airflow. The main parameters of interest in the experimental and virtual simulations include the coolant temperature, air temperature, and air pressure drop. Each of these is of interest for 1D thermal management simulations as well, which estimate and analyze the system performance. The air pressure drop through the radiator is a critical performance parameter, and has been a difficult parameter to measure in the past. In addition, defining any theoretical equations for the contributions to this pressure drop has proved challenging, but with modern day 3D CFD techniques, this task has been made easier [21].

In the following sections, a stand-alone heat exchanger experimental setup is discussed and conditions replicated, as close as possible, in the 3D simulations. A short discussion on the results will follow.

4.2 Experimental Measurements

A room-sized calorimeter test bench was used for the stand-alone radiator testing. The radiator is a cross-flow single-pass flat tube and fin radiator, with a frontal area of about 0.3 m^2 and a thickness of 16 mm; exact dimension and image are included in Figures 4.1 and 4.2.



The radiator is mounted on a duct, which contains a fan further downstream, pulling the airflow through. Upstream of the radiator, pressure and temperature are measured at the air inlet of the room. This air inlet is part of a closed-loop system, as the air passes through the downstream ducting, gets cooled down to a standard test temperature, and is fed back into the room. A simple depiction of this room setup can be seen in Figure 4.3. Note this is not to scale. Two different tests were performed with this isolated radiator experiment.

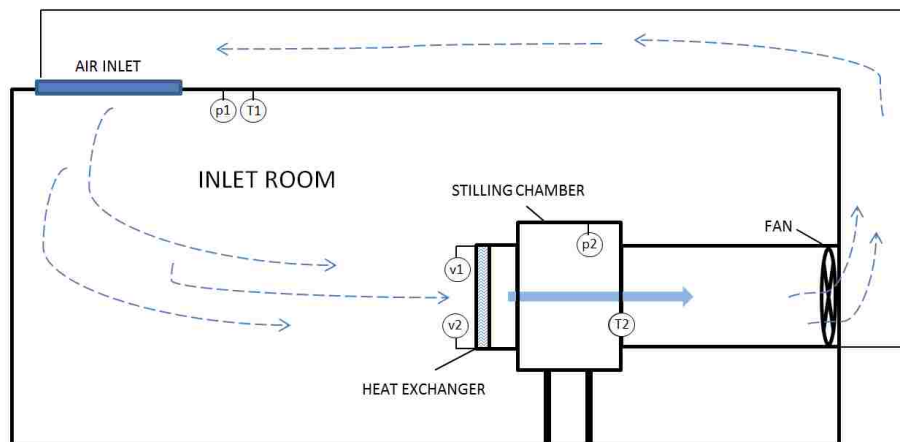


Figure 4.3: Simplified diagram of calorimeter test

The first case was considered without any heat exchange between the air (cold) stream and water (hot) stream in the radiator core. The air velocity was varied for five different values, and the pressure difference between the two pressure taps was calculated; “delta P air” in Table 4.1. The general location of the pressure measurement points is shown in Figure 4.3, by $p1$ and $p2$. Similarly, measurement locations of temperature ($T1, T2$) and velocity ($v1, v2$) are displayed as well. The air temperature downstream of the radiator is based on four temperature probes arranged in order to provide an average temperature over the flow area. The velocity is measured with two pitot tubes, and an average is calculated to report the air velocity values in Table 4.1. The reported mass flow is a calculated value. It should be noted that the velocity recorded is a standard velocity, which needs to be converted to actual at-the-radiator conditions through a density correction. The equations for this conversion are part of ASHRAE test standards, and can be found in Appendix A. Note that values with a * are measured quantities, while the mass flow rate is a calculated quantity.

	units	step 1	step 2	step 3	step 4	step 5
pressure - barometric	Pa	97788	97770	97754	97715	97649
delta P air	Pa	33.649	81.569	119.599	162.743	195.718
T air supplied	°C	316.257	316.413	316.346	316.507	316.641
T air returned	°C	316.176	316.090	316.139	316.271	316.227
delta T air	°C	-0.081	-0.323	-0.207	-0.236	-0.415
mass flow air	kg/s	0.664	1.046	1.303	1.570	1.752
velocity air - standardized	m/s	1.901	2.995	3.733	4.497	5.020

Table 4.1: Experimental test data, iso-thermal conditions

By plotting the pressure drop and velocity, the following curve is obtained.

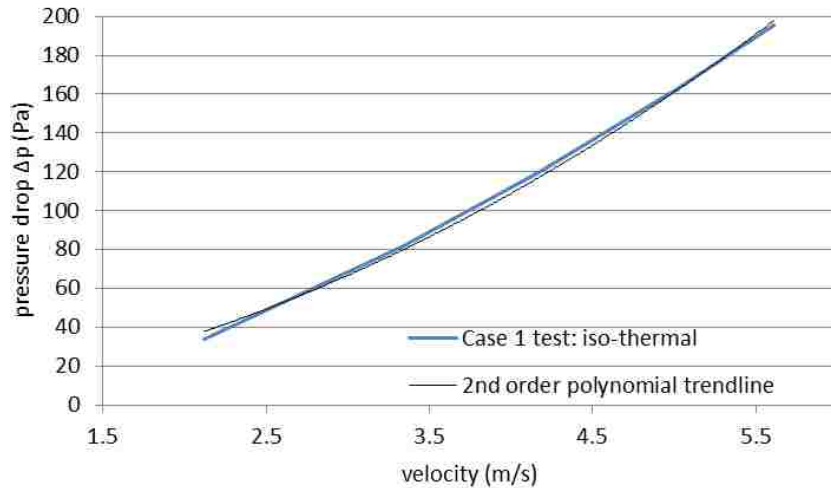


Figure 4.4: Pressure drop-velocity curve, iso-thermal conditions

By fitting a second-degree polynomial to the curve (black curve), coefficients are obtained for the inertial and viscous terms as previously described in equation (3.17). Note the small differences between the data and approximation, especially at lower velocities. These coefficients represent the pressure drop at specific inlet velocities for the heat exchanger, under iso-thermal conditions.

P_i	311
P_v	456

A similar measurement procedure as described previously was undertaken for the second case of testing. This test however, introduced a water flow rate in the radiator core, and thus heat transfer between the two fluids. Additional measurement data for the hot tube-side fluid is therefore required.

This test involved a “matrix” of air and water flow rates. The end result was a table with five different airflow rates, each tested at five different water flow rates, resulting in a total of 25 test points. A sample test point is shown below, with water-side data and a total heat transfer rate calculated, based on an average of the two fluids.

pressure - barometric	Pa	97930
delta P air	Pa	131.968
T air supplied	K	316.677
T air returned	K	347.311
delta T air	K	30.634
mass flow air	kg/s	1.304
velocity air - standardized	m/s	3.736
T water supplied	K	361.055
T water returned	K	354.548
delta T water	K	6.507
mass flow water	kg/s	1.480
Q air	KW	40.231
Q water	KW	40.224
Q average	KW	40.228

Table 4.2: Experimental test data step 14, with heat transfer

By once again plotting the pressure drop - velocity curve for the case with heat transfer, the following porous coefficients (dimensionless) are obtained,

P_i	339
P_v	506

This curve is shown in Figure 4.5, along with the previously obtained curve for the iso-thermal condition. Note that under iso-thermal test conditions, the curve is referred to as *Case 1 test*, while the test with heat transfer between the two streams is deemed *Case 2 test*.

Both curves are plotted to give a visual representation of the difference in pressure drop under two varying assumptions of heat transfer.

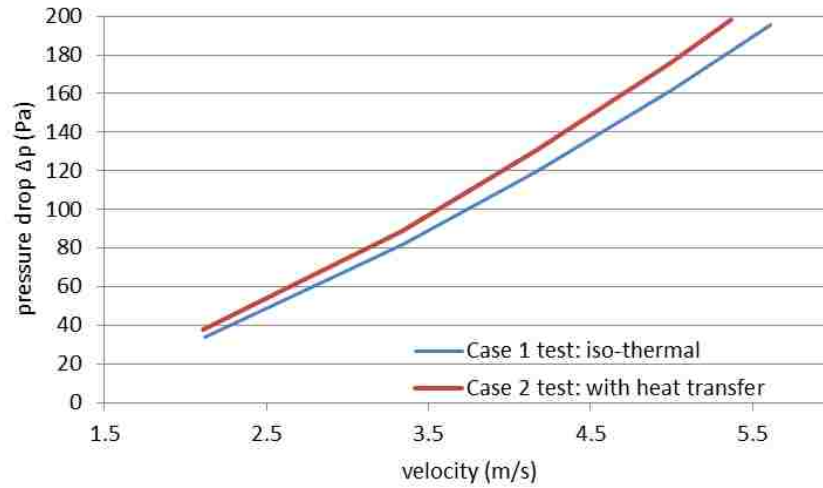


Figure 4.5: Pressure drop-velocity curves from experimental testing

The difference between the curves is significant, as the pressure drop for the same velocity is much higher in the case with heat transfer. At lower velocities, this difference is roughly 11%, while it is about 7% for the higher range of velocities. These differences are further discussed in the results section of this chapter. In the next section, the simulation procedure is explained.

4.3 Virtual Simulation

The computational tool utilised for all 3D CFD simulations, including the full vehicle simulations discussed in a later chapter, is STAR-CCM+ version 9.06. It is based on the Navier-Stokes equations and uses some of the concepts summarized in section 3, “*Computational Methodology*”.

The first step in the simulation setup is to create a CAD model representative of the real test case. As this geometry is quite simple, this was done directly in the STAR-CCM+ software. The details of this calorimeter room geometry model can be seen in Figure 4.6.

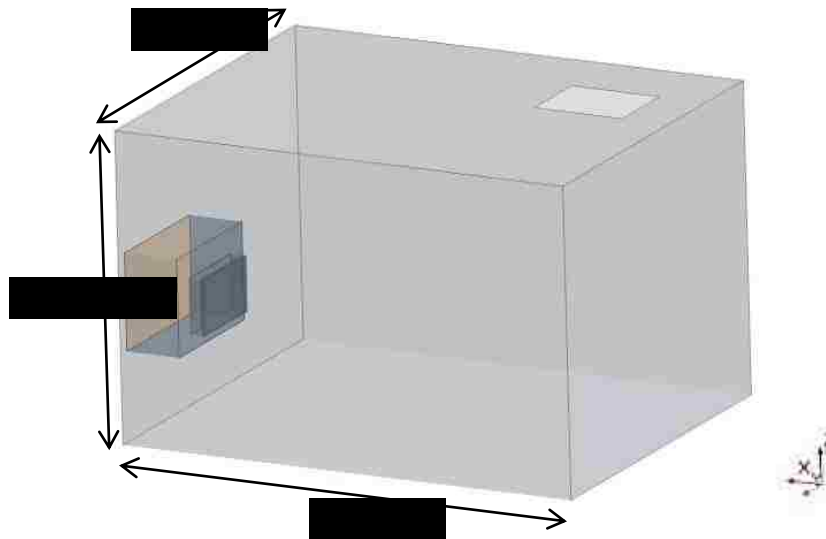
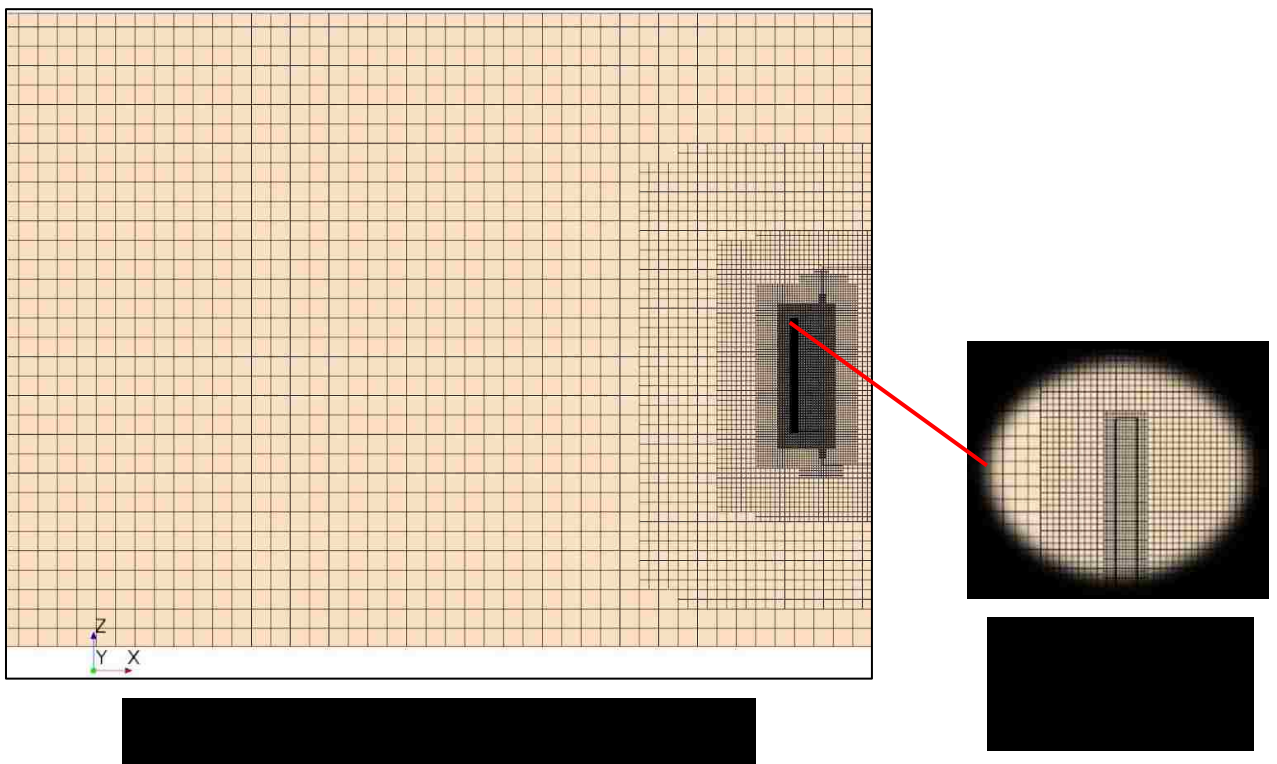


Figure 4.6: Test room geometry

Surface and volume meshes with this geometry were created directly in STAR-CCM+ also. The volume mesh was created using the Trimmed Mesher that generates hexahedral elements. In addition, a conformal mesh is created at upstream and downstream interfaces of the radiator, which can be seen in Figure 4.8. A conformal mesh aims to imprint one boundary on the other, creating a match of cell elements between two different parts. For example, the cells upstream of the radiator belonging to the inlet room are directly mirrored on the first set of elements that make up the radiator. A conformal mesh produces a high-quality discretization for the analysis, and is able to transfer data between cells more accurately, thus reducing computational cost.

Figure 4.7 shows a cross-section of the volume mesh for the entire geometry, which consists of a total of approx. 2.5 million cells with an increased cell density around the radiator region, shown by Figure 4.8. The radiator core is made up of a 2 mm cell size, which results in 7-8 cells across the core thickness. The refinement region around the radiator is 4 mm with a “medium” level outward growth rate. The room base size is 100 mm. The radiator and surrounding area refinement is responsible for ~40% of the total cell count. The isolated radiator simulation requires approximately five hours on a local machine running 12 processors.



For the air entering the room, a mass flow inlet condition was used, which also specifies the incoming air temperature. A pressure outlet boundary condition was used at the outlet chamber, which was maintained at ambient pressure. All the walls are classified as smooth, no-slip and adiabatic.

For the case in which heat transfer is included, similar boundary conditions are considered for the water-side inlet and outlet. The inlet tank was specified as a mass flow inlet, while the outlet tank was a pressure outlet. In order to restrict the water flow in the

lateral direction only (*y-direction* in Figure 4.9), resistance coefficients for the coolant core also need to be specified. As the pressure drop is not of interest for the water-side flow, the goal would be to restrict the direction of the fluid by simply choosing very high porous resistance coefficients in the *z-* and *x-direction*, and slightly less in the *y-direction*, to simulate the water flow in the direction of the tubes. Figure 4.9 shows the coolant tanks and core geometry (core dimensions as in Figure 4.1),

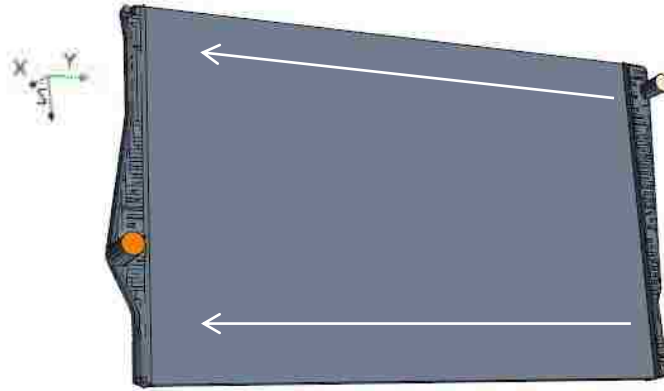


Figure 4.9: Coolant tanks and direction of water flow in radiator core

Three different scenarios were considered for the isolated radiator simulations. They are often referred to by “Case” number in this thesis, to represent the different assumptions in flow conditions. The cases are summarized in the table below:

	Description	Equation of state	Porous media coefficients (dimensionless)
Case 1	Incompressible, iso-thermal	Constant density, $\rho=1.0795 \text{ kg/m}^3$	$P_i = 311$
			$P_v = 456$
Case 2	Incompressible, with heat transfer	Constant density, $\rho=1.0795 \text{ kg/m}^3$	$P_i = 339$
			$P_v = 506$
Case 3	variable density, with heat transfer	Ideal gas, $\rho = P/RT$	$P_i = 339$
			$P_v = 506$

Table 4.3: Isolated radiator simulation parameters for each case

Note that the porous media coefficients for *Case 2* and *Case 3* are naturally identical, since only one curve was obtained from experimental testing that included heat transfer effects.

The rest of the solver settings used are the same for each case; mainly of interest:

- 3D, steady state, Reynolds-Averaged Navier-Stokes equations
- Segregated Flow solver along with the supporting Segregated Fluid Temperature energy model (in the case of heat transfer) with second order discretization schemes
- Realizable k- ϵ two-layer turbulence model, with two-layer all- y^+ wall treatment
- Dual-stream ‘actual’ heat exchanger model, modeled as a porous media with different porous resistance coefficient terms under “cold” and “hot” conditions

In the next section, the results of each simulation case are analyzed and compared to experimental testing.

4.4 Results and Discussion

For the iso-thermal case only, the main focus is on the pressure drop characteristics to validate the simulation. This relatively simple iso-thermal simulation allows a focus on the geometry and porous media accuracy, without any other complexities for now. Table 4.4 shows the simulation and experimental results:

	units	step 1	step 2	step 3	step 4	step 5
delta P air - experiment	Pa	33.7	81.6	119.6	162.7	195.7
delta P air - simulation	Pa	37.6	79.7	116.4	161.8	197.1
error	%	-10.6	2.4	2.7	0.6	-0.7

Table 4.4: Correlation of radiator pressure drop

The simulated pressure drop has a good correlation with experimental results. This simply confirms the implementation and behaviour of the porous media model for the heat exchanger. It also confirms the simulation setup, such as the geometry, boundary conditions, and specified physics. Figure 4.10 shows the results of the simulated pressure drop curve compared to the pressure drop curve obtained from experimental testing.

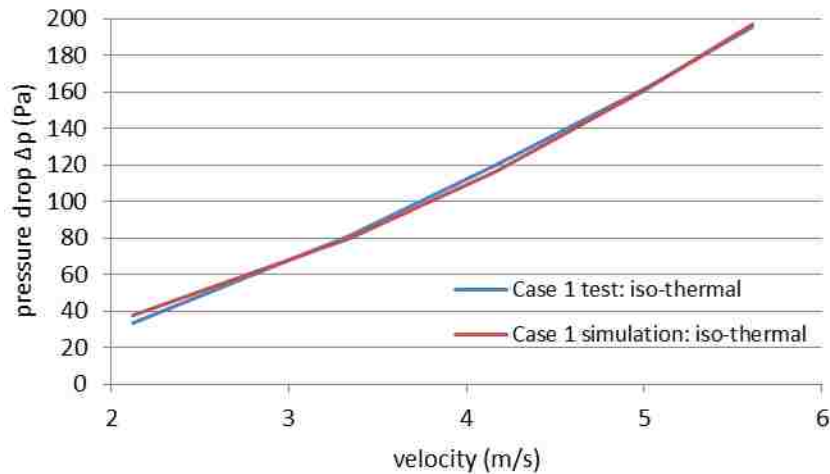


Figure 4.10: Correlation for pressure drop for Case 1 iso-thermal conditions

Using the porous resistance terms as defined for the iso-thermal case shows good correlation between experimental and simulation results. The higher percent error in *Step 1* is an unexpected outcome based on the low error achieved in the other steps. However,

this higher error is attributed simply to the misrepresentation of a second order polynomial curve of the experimental data, as was shown in Figure 4.4. The curve fit is forced to intercept at $(0,0)$ in order to obtain two coefficients for the porous media representation. At low flows, this $(0,0)$ intercept is not ideally representative and therefore the simulation results show a slight over-estimation of pressure drop. However, this is the current procedure to estimate porous media behaviour in several software codes. At higher velocities, this error is almost diminished.

Due to the nature and geometry of the experimental setup, undesired pressure losses are present that are not reflective of the heat exchanger “core-only” pressure drop. These losses will be addressed in the following pages. To aid in the explanation of these pressure losses, the following equation is presented (Kakac and Liu, 1998) [37],

$$\Delta p = \Delta p_i + \Delta p_c + \Delta p_a + \Delta p_e$$

$$= \frac{G^2}{2\rho_i} \left[(1 - \sigma_i^2 + K_c) + f \frac{4L}{D_h} \left(\frac{\rho_i}{\rho_m} \right) + 2 \left(\frac{\rho_i}{\rho_e} - 1 \right) - (1 - \sigma_e^2 - K_e) \left(\frac{\rho_i}{\rho_e} \right) \right]$$

where G represents the mass flux of the fluid, and σ the passage area ratio. The reader is referred to the nomenclature for further explanation of the other terms.

The first contribution, Δp_i , is due to an abrupt contraction in flow area (from the room to the radiator), and is termed the entrance loss. This term is obtained by considering Bernoulli’s equation with a loss coefficient K_c , combined with the mass conservation law,

$$P_1 + \frac{1}{2} \rho V_1^2 = P_2 + \frac{1}{2} \rho V_2^2 (1 + K_c)$$

If,

$$\sigma = \frac{A_2}{A_1} \quad G = \frac{\dot{m}}{A}$$

Equation (4.2) eventually leads to,

$$\Delta P = \frac{1}{2} \frac{G^2}{\rho_i} (1 - \sigma^2 + K_c)$$

A similar procedure is undertaken for the exit loss term, Δp_e .

Approximations of inlet (contraction) loss coefficient K_c and exit (expansion) loss coefficient K_e have been made in several sources of literature, such as White [43] and Kays and London [38]. These loss coefficients have their origins in the observation of pipe flow. Figure 4.11 shows K_c and K_e through a rectangular passage as a function of the area contraction ratio σ , for different Reynolds numbers.

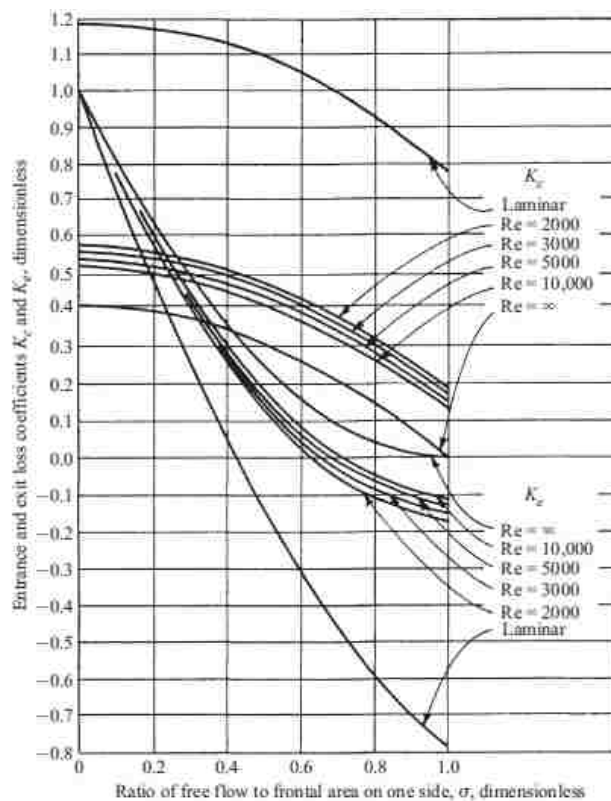


Figure 4.11: Loss coefficients as a function of area contraction ratio for different Reynolds numbers, from Kays and London 1984 [38]

The remaining two terms in equation (4.1) make up the pressure losses occurring in the heat exchanger core. The Δp_c term is the pressure loss due to friction effects through the radiator channels. It is written here in terms of the Fanning friction factor f which can be approximated as:

$$f = \frac{\tau}{\rho \frac{u^2}{2}}$$

Note that the Fanning friction factor is one-fourth of the Darcy friction factor.

The last term, Δp_a is obtained by a momentum balance across the core of the radiator, to take into account possible density changes and therefore acceleration/deceleration of the flow in the core. The pressure loss due to a momentum change in the core,

$$\Delta p_a = \frac{\dot{m}}{A_c} (V_2 - V_1)$$

which can be re-written in terms of density and the mass flux G , where

$$V = \frac{G}{\rho}$$

Therefore,

$$\Delta p_a = G^2 \left(\frac{1}{\rho_e} - \frac{1}{\rho_i} \right)$$

This is especially applicable to gas flows, where density is strongly influenced by temperature changes. Note with regards to the current discussion based on iso-thermal conditions, the density terms do not have an effect. However, this will naturally change when heat transfer is introduced and thus there is a density difference between the inlet and outlet of the core.

For the inlet loss, equation (4.1) takes into account the inlet contraction loss. While this is most likely the greatest contribution to the total upstream inlet loss, there are additional losses present not captured in the above equation as specific to this experimental setup. One of the sources comes from friction losses occurring around the radiator edges. The flow pattern is shown in two dimensions in Figure 4.12, and is present around the entire frame of the radiator. These friction losses are sometimes referred to simply as edge losses.

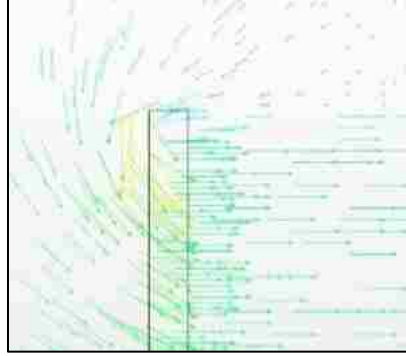


Figure 4.12: Vector plot illustrating inlet edge losses around radiator frame

From Gullberg [31] and Walter [44], similar experimental setups show a bellmouth duct opening adopted upstream of the test component. This would assist in guiding the flow towards the core and would significantly reduce the friction losses present. Another contribution stems from friction losses at the wall boundaries. This is not only present upstream of the radiator at the inlet room walls, but also downstream at the wall boundaries of the duct.

The exit losses captured due to expansion of the flow in equation (4.1) can be analyzed by looking at the terms σ and K_e . The cross-sectional area of the duct directly downstream of the radiator is consistent with the radiator area itself. This means,

$$\sigma = \frac{A_2}{A_1} = \frac{A_{core}}{A_{downstream}} \approx 1$$

For the exit coefficient K_e , a dependency on Reynolds number is present, but it is a relatively weak dependence, as can be seen in the graph from Figure 4.10. As an approximation for K_e , the curve $Re = \infty$ can be used and consequently, equation (4.9) applies,

$$K_e = (1 - \sigma)^2$$

If the term $\sigma \approx 1$, the coefficient $K_e \approx 0$. The end result is a negligible exit loss term Δp_e altogether for this particular geometry. A little further downstream, there is a slight change in duct cross-sectional area where this expansion effect is present, but is again assumed minimal due to $\sigma \approx 1$. The magnitude of this term would be larger if the

downstream geometry was an open room, as this would result in total loss of dynamic pressure. In this case, the assumption is made that most of the dynamic pressure is retained; total pressure losses from the rear face of the radiator to the pressure measurement point p_2 (see Figure 4.3) are mostly a result of friction losses at the wall boundaries with some small contribution due to expansion.

All the pressure losses discussed up to this point, as mentioned previously, are difficult to quantify, especially with the limited information from experimental measurements. For this reason, the CFD simulations can be used to understand the underlying physics in more detail, and provide further information on the magnitude of the pressure losses upstream and downstream, including contributions not captured in equation (4.1).

From the iso-thermal CFD simulation, total pressure values were reported at different locations in the flow. These were surface-averaged total pressure values over a given cross-section, such as the inlet boundary interface (pt1 in Figure 4.13) and the radiator front interface, pt2. The difference in pt1 and pt2 should give the total inlet losses, consisting of effect A, B, C, and D. These contributions are summarized below.

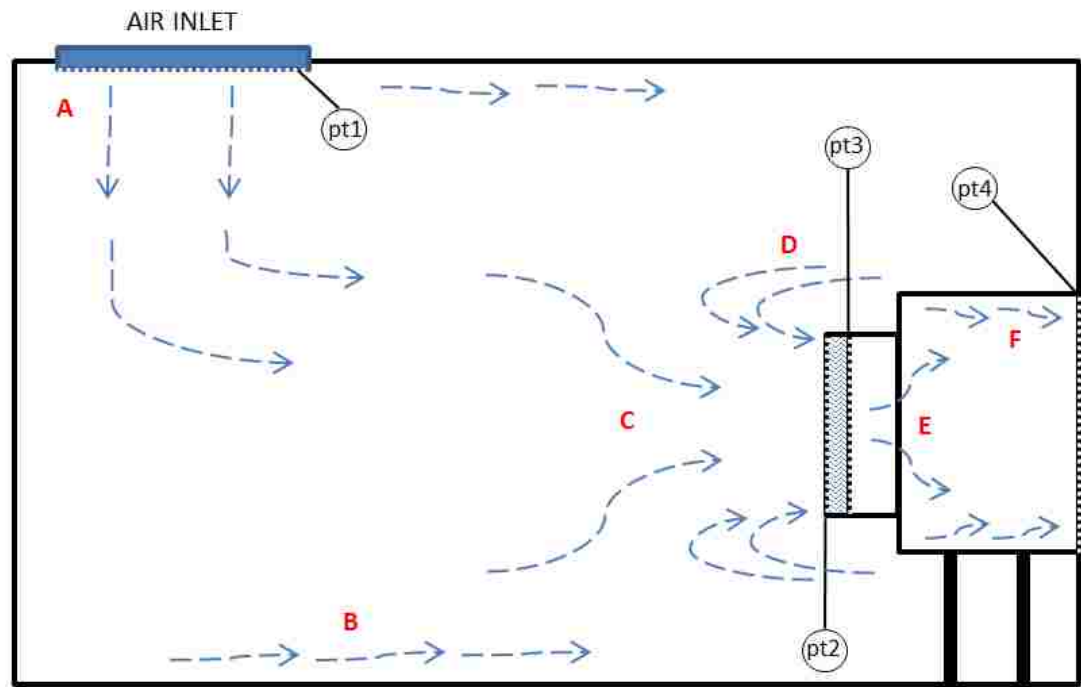


Figure 4.13: Summary of total inlet and outlet losses in isolated radiator experiment

- Total inlet losses consist of effects at:
 - A:** although not discussed in detail, this is due to the momentum loss of velocity in the z -*direction* as it enters the room and travels through to the radiator.
 - B:** friction at the wall boundaries in the inlet room
 - C:** a flow area contraction from inlet room to radiator core
 - D:** friction around the radiator edges (edge losses)

The total inlet loss (Pa) was calculated by reporting the difference in total pressure between the inlet boundary pt1 and the radiator front interface pt2
- Total outlet losses consist of effects at:
 - E:** area expansion from downstream of the radiator to ‘second’ duct
 - F:** same as in B; friction at the wall boundaries in the downstream duct

The total outlet loss (Pa) was calculated by reporting the total pressure between the radiator rear interface pt3 and the outlet boundary pt4.

Table 4.5 summarizes the inlet and exit losses for each iso-thermal simulation, consisting of five different conditions and flow velocities. As a reminder, these steps 1-5 are summarized in Table 4.1.

	Total pressure drop	Total loss due to inlet (pt1 to pt2)		Total loss due to exit (pt3 to pt4)		Calculated "core-only" loss	
	Pa	Pa	% of total	Pa	% of total	Pa	% of total
Step 1	37.64	3	8	1.7	4.5	32.94	87.5
Step 2	79.65	7	8.8	4	5.1	68.65	86.2
Step 3	116.41	11	9.4	6	5.2	99.41	85.4
Step 4	161.84	15	9.3	9	5.6	137.84	85.2
Step 5	197.07	19	9.6	11	5.6	167.03	84.8

Table 4.5: Inlet and outlet pressure losses from simulation analysis

The contribution of the core-only loss, which includes the terms Δp_a and Δp_c from equation (4.1), makes up about 85-87% of the total pressure loss. This is in agreement with other experiments from literature sources, such as Kakac and Liu [37] and Kays and London [38], albeit slightly lower than the reported 90%+. This could simply be due to test or geometry setup, and lower losses associated with upstream and downstream conditions of the heat exchanger.

The total inlet loss and outlet loss contribute approximately 8-10% and 4-6% of the total pressure loss, respectively. This results in an over-estimation of the core-only pressure drop by about 14-18% with current methods; that is, by taking the pressure drop reported from experimental testing without any corrections for losses and applying these values directly to the porous media via resistance coefficients.

The discussion will now move to the case in which heat transfer effects are included, but still under the assumption of constant density; *Case 2* in Table 4.3. As mentioned, it is assumed that similar pressure losses are present as discussed above and the core-only pressure drop is over-estimated by a similar margin. With the dual-stream heat exchanger model used in the ‘hot’ (with heat transfer) simulations as discussed in section 3.6, an additional parameter can be used to validate the CFD simulations; temperature. It is possible with this model to predict coolant temperature drop and air temperature increase through the radiator core, and therefore heat transfer rate as well.

The relevant parameters used to compare simulation and experimental results are shown in Table 4.6. This table shows the result of a single test condition.

	Δp air (Pa)	ΔT air (K)	ΔT water (K)	Q (heat transfer rate) averaged (kW)
Simulation	127.11	30.19	6.71	39.91
Experimental	131.9	30.63	6.53	40.23
Percent error	3.8%	1.5%	2.7%	1.0%

Table 4.6: Results of simulation Case 2, incompressible with heat transfer

As a preliminary conclusion, this table shows that using a porous media approach with a dual-stream heat exchanger model, it is possible to obtain good results as compared to the experimental measurements.

Recall that the porous resistance coefficients used in the iso-thermal simulation *Case 1* are different than *Case 2* resistance coefficients, as summarized in Table 4.3. In the case with heat transfer, the coefficients are greater in magnitude in order to capture the additional pressure drop that occurs when energy is added to the airflow. Equation (4.1) is shown here again in order to aid in the explanation for this.

$$\Delta p = \Delta p_i + \Delta p_c + \Delta p_a + \Delta p_e$$

$$= \frac{G^2}{2\rho_i} \left[(1 - \sigma_i^2 + K_c) + f \frac{4L}{D_h} \left(\frac{\rho_i}{\rho_m} \right) + 2 \left(\frac{\rho_i}{\rho_e} - 1 \right) - (1 - \sigma_e^2 - K_e) \left(\frac{\rho_i}{\rho_e} \right) \right]$$

Regarding total inlet losses and total outlet losses, including the ones previously discussed that are not captured in the above equation, a similar procedure was undertaken as with the iso-thermal simulation; the pressure losses upstream and downstream were evaluated with CFD simulations and recorded in a similar manner as Table 4.5. The results revealed that total losses upstream of the radiator and total losses downstream of the radiator were similar in magnitude (Pascal) as with the iso-thermal case.

Upstream flow conditions remain the same and thus no difference is expected. For the downstream condition, the density term (ρ_i/ρ_e) now plays a role, which is to magnify the term containing σ and K_e . However, the same assumptions regarding minimal area change in the downstream duct apply, and therefore the pressure loss term Δp_e becomes altogether negligible.

The conclusion is that the additional pressure drop comes directly from the core, where the cells belonging to the air and water region contain energy source/sink terms. This is the only change in the simulation; the addition of a heat exchanger model. The density ratio terms become significant, as both terms Δp_c and Δp_a are magnified i.e. multiplied by a ratio greater than 1 (instead of unity as in *Case 1*).

In addition, the friction factor will change as a result of its dependency on Reynolds number, which is of course also dependent on viscosity with the introduction of

temperature changes. With an increase in temperature, the viscosity of air will increase, thus reducing the Reynolds number and increasing the friction factor. This can also be seen in Figure 4.14, data obtained from Kays and London [38] on some louvered fin compact heat exchangers.

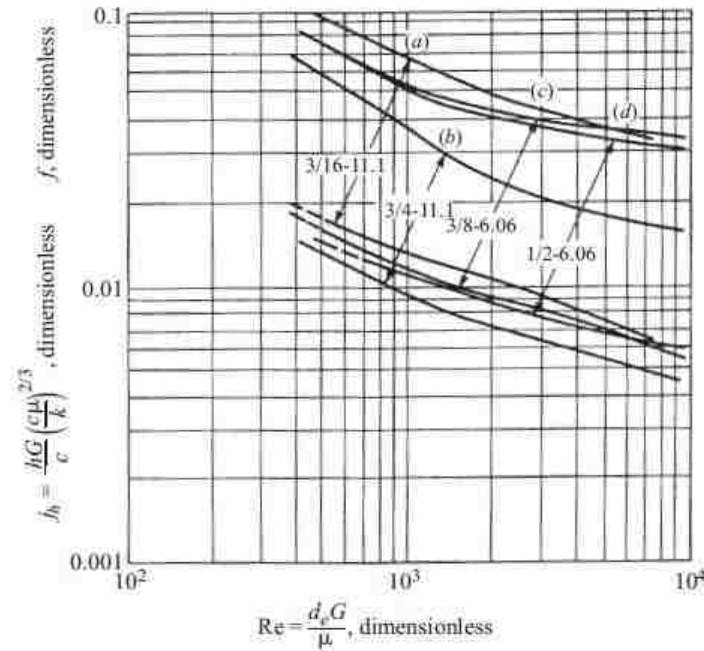


Figure 4.14: Heat transfer and flow friction characteristics for a sample of louvered fin compact heat exchangers, from Kays and London (1984) [38]

The addition of heat transfer and its influence on the above parameters is most likely responsible for the majority of the increase in pressure drop value.

Despite this analysis on heat transfer and density terms to explain the additional pressure drop, none of these effects can be realized through the CFD simulations. *Case 2* was run incompressible, and thus with a constant density. These effects reflect the expected flow behaviour in a real situation, where such a density change exists in the core due to heat addition, and therefore an increase in core velocity must follow to satisfy the conservation of mass law. For this reason, in an attempt to capture these flow effects in the CFD simulation, a variable density simulation was tested.

Case 3 uses the ideal gas law as an equation of state to relate density to pressure and temperature. The same porous resistance coefficients as in *Case 2* are adopted, since heat

transfer effects are still included. Table 4.7 includes the results of the variable density run *Case 3*, with consistent use of boundary conditions:

	ΔT air (K)	ΔT air - error	ΔT water (K)	ΔT water - error %	Q heat transfer rate (kW)	Q heat transfer rate - error
Experimental	30.63	-	6.53	-	40.23	-
Case 2 Simulation	30.19	1.5%	6.71	2.5%	39.91	1.0%
Case 3 Simulation	30.02	2.0%	6.62	1.4%	40.90	1.6%

Table 4.7: Simulation results compared to experimental testing for Case 2 and Case 3 from Table 4.3

The error observed in the air pressure drop must mean there is some unaccounted-for effect in the variable density simulation which over-estimates this pressure drop. Figures 4.15 and 4.16 show the difference in pressure drop for the experimentally obtained curve and the simulated results, for *Case 2* and *Case 3*, respectively. Note that *Case 2 test* and *Case 3 test* refer to the same curve, as only one curve (and therefore one pair of porous terms) is obtained from experimentally testing with heat transfer. Figure 4.16 therefore demonstrates the over-estimation in pressure drop for the *Case 3* simulation when applying the pressure curve obtained from experimental testing.

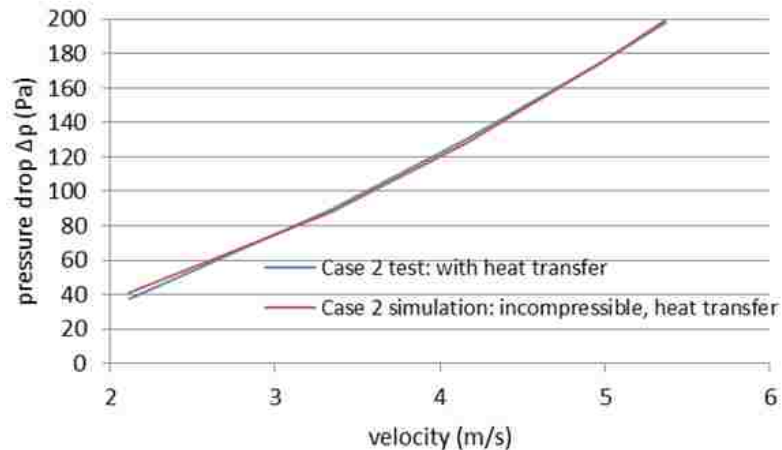


Figure 4.15: Correlation for pressure drop for Case 2; incompressible with heat transfer

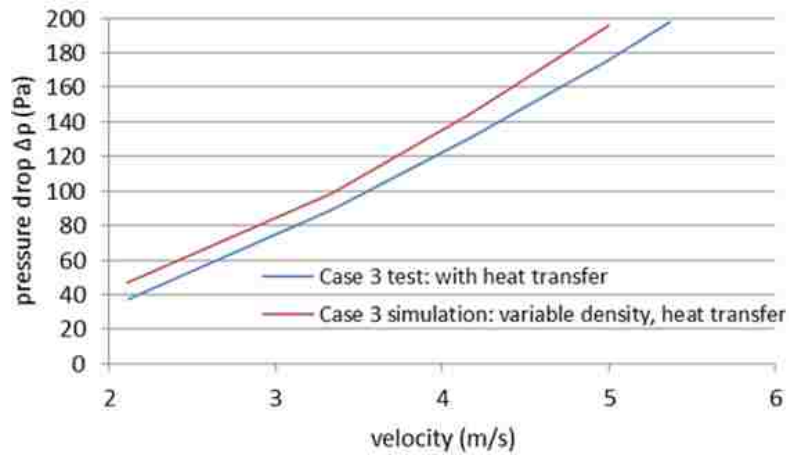


Figure 4.16: Correlation for pressure drop for Case 3; variable density with heat transfer

The expected velocity increase and density change through the radiator core however is accounted for and is summarized below:

- Velocity increase of 9.2 % from front interface of the radiator to rear
- Density change (decrease) of 8.8 % from front interface of the radiator to the rear

The reason for the large differences in pressure drop in *Case 3* is attributed to the following: the pressure drop Δp -velocity (v) curve provided as an input to the simulation (curve *Case 3 test* from Figure 4.16) already captures the effects of temperature on the airflow. That is, the temperature increase of air results in an increase in local velocity and therefore in an increase in heat exchanger pressure drop. This is because the calculation for the core pressure drop may not be a function of only one velocity.

Since these effects are captured in the porous coefficient terms used as the input, further influence from temperature on density and viscosity should be avoided. In this case however, by using the curve from experiment as an input and performing the simulation under the ideal gas assumption, the terms as outlined in equation (4.1) that cause an increase in pressure drop due to temperature are accounted for twice. In [21], the author mentions the need to avoid accounting for thermo-physical properties twice when applying porous coefficient terms. It follows that the porous terms should in fact be defined or converted to adiabatic conditions when running an ideal gas law assumption

and including heat transfer in the heat exchanger core. This may explain perhaps the minimal difference between the iso-thermal conditions *Case 1* curve and variable density hot conditions *Case 3* curve, as shown in Figure 4.17. However, it was observed that in this simulation, the more accurate method is to compute an additional and more representative curve for *Case 3*. Using coefficients from the iso-thermal simulation still results in a considerable error when compared to experimental data.

It is possible therefore to find porous resistance terms which will be suitable for the variable density simulation only. The process of finding the correct coefficients was obtained by working in the other direction; i.e. finding which coefficients will give the desired pressure drop for the velocity as observed in the simulation. The coefficients for the variable density simulation with heat transfer requires the porous inertial coefficient $P_i = 325$, and the porous viscous coefficient to be $P_v = 336$. This gives pressure drop results that are comparable to experimental data, while the rest of the relevant parameters such as ΔT_{air} and ΔT_{water} remain unchanged. The author acknowledges the fact that the new porous coefficients obtained for the variable density do not seem to follow a clear trend when compared to the other simulation cases, which are summarized in Figure 4.17. It is difficult to interpret the relative importance of each term. It should also be mentioned that the initial assumption of using the iso-thermal coefficients from *Case 1* in the variable density simulation *Case 3* still produced an over-estimation of pressure drop, and that therefore the only other method was to perform the variable density simulations and use the results to obtain a curve.

Figure 4.17 is a summary of the pressure drop-velocity curves and corresponding porous media terms required for each simulation case thus far discussed. Applying these terms gives results reflective of experimental testing within a reasonable degree of error. The error is most pronounced at low velocities, caused by the second degree polynomial fit required to characterize the porous media behaviour in STAR-CCM+.

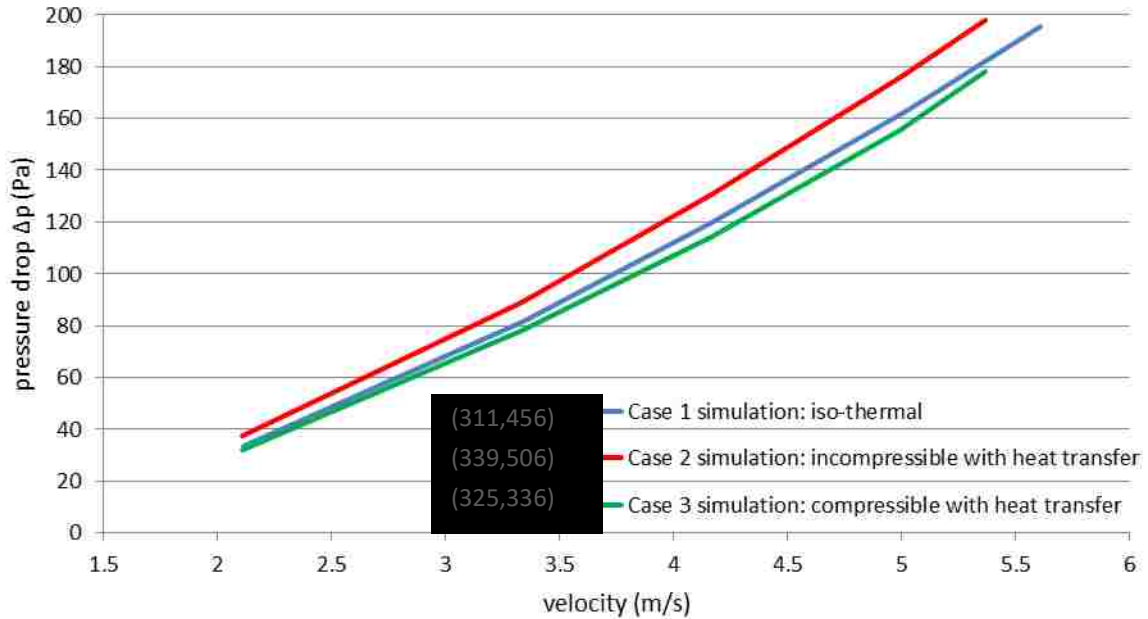


Figure 4.17: Pressure drop-velocity curves for all isolated radiator simulations; Case 1,2,3 with porous media coefficients (P_i , P_v)

Note that *Case 1* and *Case 2* in Figure 4.17 are representative of the curves obtained directly from experimental testing.

With regards to performing a variable density simulation, the additional requirement of finding new porous media terms, although not overly burdensome, is a task not required in the other two simulation cases. In addition, the slight increase in computational time (+5%) to reach convergence with the variable density case with the ideal gas law may prove to be unnecessary. *Case 2* (incompressible) was adequate to be able to validate the porous media as well as the dual-stream heat exchanger. It is true that the local decrease in density and increase in velocity at the heat exchanger is not captured in a constant density scenario, but mass flow rate is often the parameter of interest in heat exchanger analysis. In any case, the procedures and assumptions for each simulation case have been outlined in this chapter. A dual-stream radiator can now be incorporated in a full vehicle underhood simulation with a degree of surety. Similar concepts discussed in this chapter will be applied to a full vehicle underhood model, along with the rest of the underhood components, including other heat exchangers and a fan model.

5. FULL VEHICLE MODELLING

5.1 Introduction

CFD methods have been extensively adopted in recent years for the design of the vehicle thermal management system. The complex underhood airflow and its interaction with multiple components present a need to study both the aerodynamic and thermal domains. In order to perform a comprehensive flow-thermal analysis, a combination of 1D and 3D methods is the widely/commonly adopted approach in industry. Several sources outlined in the literature review have used similar approaches, see section 2.2. As mentioned previously, 3D simulations are used to characterize and show the details of the flow, while 1D simulates the system level thermodynamic performance. The focus of this thesis is on the 3D modelling.

The validation of the simulations can be accomplished in some cases with stand-alone component testing, as performed with the radiator in Chapter 4. However, individual testing does not provide a full picture of the complete cooling system performance. To understand the effects of various components and geometries, it is ideal to perform testing of the complete underhood packaging. Some studies, as discussed in section 2.2, perform tests based on simplified geometries, including only a portion of the underhood, while others are able to capture the full internal flow and external aerodynamics of the vehicle with a full model. The testing conducted here is based on full vehicle geometry. Full vehicle testing can provide a vast amount of information on the vehicle cooling system, as well as valuable information to correlate with full vehicle simulations. However, it should be noted again that the focus in this thesis is based on simulation methods early in the vehicle development cycle. While detailed geometry, underhood packaging and component performance may not be available at this point, a prediction to meet early vehicle needs is possible.

The goal of this thesis is re-iterated here: to use available data and improve currently implemented processes for the development of future vehicle underhood compartment simulations. This is achieved by studying different techniques of modelling vehicle

underhood components and investigating heat transfer effects on the cooling airflow, under different flow assumptions. Ultimately, parameters such as velocity or mass flow can be evaluated at various underhood components.

This chapter will follow a similar structure as in Chapter 4; experimental results and virtual simulations techniques will be discussed, with a results section discussing validation of the simulations and certain parameters of interest.

5.2 Experimental Measurements

The full vehicle experiment was performed in a climatic wind tunnel. Climatic wind tunnels are capable of simulating a wide range of conditions, ranging in some cases from -50°C to $+60^{\circ}\text{C}$, with solar, rain, and snow simulation capabilities. It is also possible to simulate wind speeds up to 250 km/hour. In this test facility, the floor is made up of a full-scale chassis dynamometer, or in other words a ‘rolling floor’. This allows vehicles to be tested under various driving loads and speeds. Development in climatic wind tunnels allows further insight into cooling capabilities of the engine and auxiliary components, leading to improvements in the vehicle performance and efficiency. Figure 5.1 shows a simplified diagram of the testing facility. This wind tunnel is of the closed-loop return type. Air is conducted by a series of turning vanes, and can undergo cooling through various heat exchanger stages as it is fed back to the fan, and re-circulated again to the test section. The temperature and velocity of the air is therefore controlled.

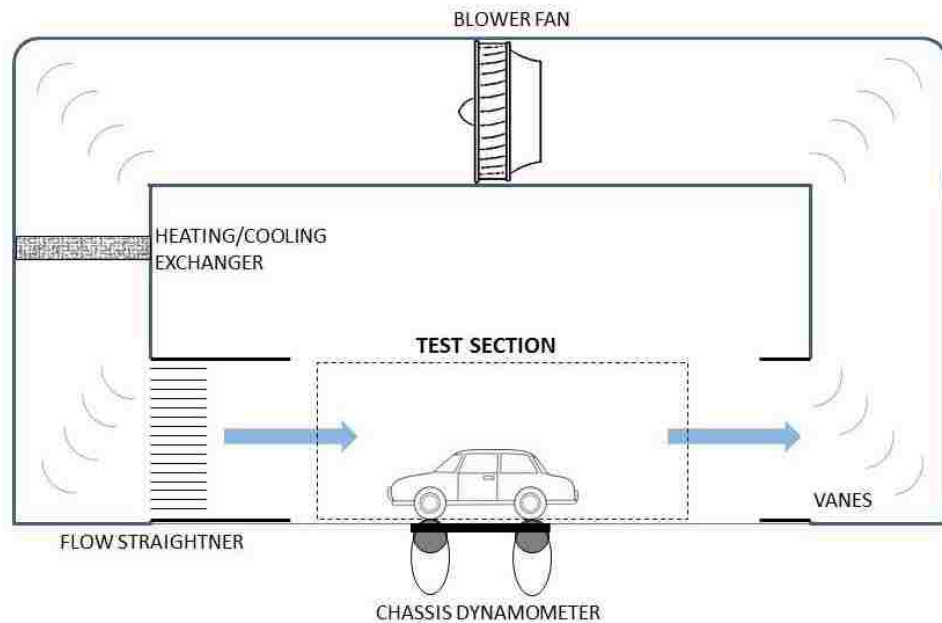


Figure 5.1: Simplified schematic of climatic wind tunnel test



Figure 5.2: Climatic wind tunnel testing area

The specific test performed for this thesis is based on road GPS data from the Davis Dam on the Colorado River. The Davis Dam road test is a commonly known test at which to evaluate the powertrain and cooling system under critical loads, and is part of standard SAE towing test procedures. The maximum elevation on this stretch of road is about 1000 m (3500 ft) at a maximum grade of 12%. For this specific test however, only a portion of the road is used, at which the average grade is about 4.5 % during the uphill section. Figure 5.3 shows the vehicle rpm over time, which can provide further insight on the specifics of the test.

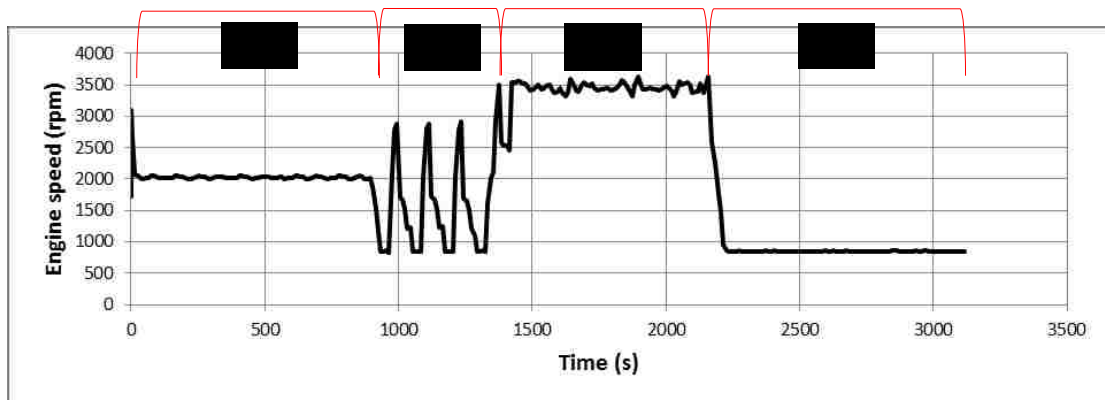


Figure 5.3: Vehicle experimental road test - engine speed vs. time

The different stages of this graph show:

- 1: steady flat-road driving condition, at approximately 89 kph (55 mph)
- 2: stop-and-start conditions, repeated three times to mimic stop signs and/or traffic lights
- 3: low gear, high load driving condition (hill-climbing) at average grade of 4.8 %, vehicle speed maintained at 89 kph (55 mph), fan at highest rpm during test
- 4: idle condition, fan rpm maintained until end of test

Low vehicle and high fan speed operation representing a hill-climbing condition is regarded as the most severe operating condition for the cooling system performance. On the other hand, aerodynamic performance is typically evaluated at higher vehicle speeds on a flat road. In this thesis, the cooling system capabilities are of interest, and simulations are performed based on operating conditions during the hill-climbing portion. Therefore, the information available on the cooling system will be extracted based on this portion of the test, between approximately $t=1500$ s and $t=2000$ s. Instead of choosing an arbitrary point, averaged values are obtained of the data during this period. The data obtained will be used for various inputs to the simulation, such as inlet conditions, and will also be used to validate the simulations. Table 5.1 shows the averaged data.

Coolant mass flow rate (kg/s)	Coolant inlet temperature (K)	Coolant outlet temperature (K)	Coolant temperature change ΔT (K)	Heat Rejection (W)	Wind speed (kph)	Inlet air temperature (K)	Fan rotational speed (rpm)
1.02	379	369.5	9.5	35255	78.3	311.1	2531

Table 5.1: Averaged vehicle test data

In order to accurately represent the third portion of the test in the wind tunnel, several aspects need to be considered. The airflow velocity entering the vehicle is not the same with a flat-road driving condition and an uphill grade. In order to account for this, a tailwind is introduced, which in fact simply reduces the incoming wind speed. This explains the difference in ‘vehicle speed’ and ‘wind speed’ in Table 5.1. In [21], it was

estimated that slight inclinations (as low as 1.5 cm between front and rear inclinations of the vehicle) can cause temperature increase of up to 20% in some air zones in some locations due to the lower airflow velocity entering the vehicle.

Note that airside parameters of interest, such as pressure drop and temperature, are not measured in this experimental test. While several measurements techniques exist, such as Particle Image Velocity (PIV), Laser Doppler Velocimetry (LDV), and anemometers for velocity measurements and thermocouples/probes for temperature measurements, the existence of such large number of components in the underhood compartment in combination with high degrees of non-uniformity presents challenges in obtaining the airside parameters with a certain degree of accuracy. This is also supported by [21]. Positioning of the measuring devices also makes for a difficult task as there is very limited space in between heat exchangers. For instance, one of the more common approaches is to use vane anemometers. This method has been applied by Regin et al. [6], Shimizu et al. [45] and several others to attempt to measure the airside parameters. However, several uncertainties exist, such as the fact that to get the correct velocity distribution, many anemometers need to be introduced over the radiator face. This results in blockage of the air and will further impose a non-uniform flow field. In addition, anemometers tend to perform poorly in higher temperature conditions as based on past experimental testing experience. The result is that in order to compare the experimental test data with simulations, one must rely on the coolant temperature change in this case, as the most reliable validation parameter and since other measurement methods were not implemented for this specific test.

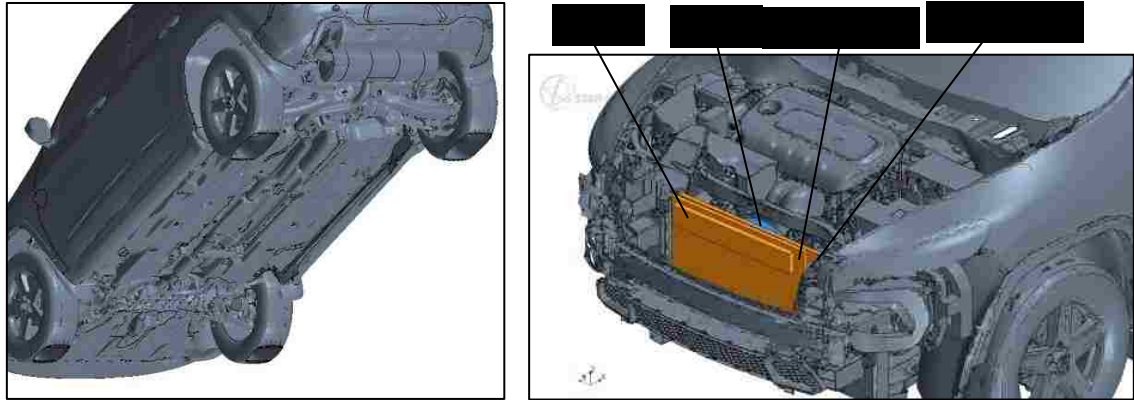
5.3 Virtual Simulation

Traditionally, the evaluation of the cooling system was done with full vehicle physical testing. However, due to the complexity of the airflow and heat transfer, it is difficult to perform reliable thermal testing, such as with methods described in section 5.2 above. In addition, experimental testing must be done with prototypes, which is expensive and can be time-consuming. With the increase in accuracy of numerical methods, it is possible to use CFD simulations to predict cooling system performance early in the vehicle development.

The full vehicle model described here includes all external surfaces, including all underbody and underhood details. In previous works such as [46, 47], simulation models include a half vehicle model or only the underhood layout. In this thesis, no changes were made from the full vehicle CAD, and underhood thermal effects are studied including the full underbody geometry. With no major pre-processing required, simulation setup time is reduced, but at the expense of an increase in cell count. This can be alleviated by ensuring cell refinement is efficiently distributed in the regions of interest.

Another advantage of full vehicle level analysis is linked to the specification of boundary conditions. Boundary conditions for different vehicle sub-systems, such as front-end and underbody, are difficult to predict with accuracy, but are not required in such a case. This also reduces simulation setup time. Otherwise, as outlined in [13], additional simulations are performed in order to solve for the inlet and outlet boundary conditions, before a simulation solving the underhood flow and thermal field can be solved.

Figure 5.4 illustrates the various geometrical features included in this model.



For the radiator, the reader is referred to Chapter 4 as similar modelling techniques are adopted in the full vehicle simulation. Instead, the next pages will focus on the other cooling modules present in the vehicle. Additional modelling techniques are required in order to account for the performance characteristics of the TOC, condenser and fan.

The TOC and condenser use a similar approach, in that both are modeled as porous media and use the single-stream heat exchanger configuration, for which a heat source is specified in Watts (W). This relatively simpler heat exchanger method is described in section 3.6, and requires less input information and no additional geometry manipulation as compared to a dual-stream model. There are several reasons for using this type of heat exchanger which aids to simplify the overall modelling.

The TOC is the first heat exchanger the airflow encounters, and therefore influences the downstream flow conditions entering the other heat exchangers. However, this influence is minimized due to its relatively smaller surface area and heat exchange rate as compared to the condenser and radiator. This can be seen in Figure 5.4b, which shows the cooling module setup in the underhood. In addition, the transmission oil temperature change is not of interest in this thesis, and for this reason a simpler heat exchanger model is adopted.

The pressure drop characteristics and heat transfer performance for the TOC and condenser are obtained directly from supplier data sheets. The added complexity with respect to the modelling and testing of a condenser is the phase change that occurs within

the tube-side fluid. For testing, this would require new measuring techniques not currently implemented at the test facility, and therefore separate condenser testing was not conducted. From the simulation perspective, the phase change introduces more complex physics for yet another fluid. This would increase computational time considerably. In result, the decision was made to model the condenser similar to the TOC, by specifying a heat source without a prediction of hot fluid temperature changes.

For the TOC and condenser, heat transfer rate is also provided by the supplier for varying airside mass flow rates, Figure 5.5. The airflow for each heat exchanger is an unknown quantity when setting up the simulation model, and would require an iterative process to obtain the desired heat transfer from the heat exchangers. To avoid performing multiple simulations, a look-up table is provided for the heat transfer rate based on the graphs shown in Figure 5.5. This table updates the heat source of the TOC and condenser with the flow field until a steady value is achieved. The look-up tables for the TOC and condenser are provided in Appendix B.

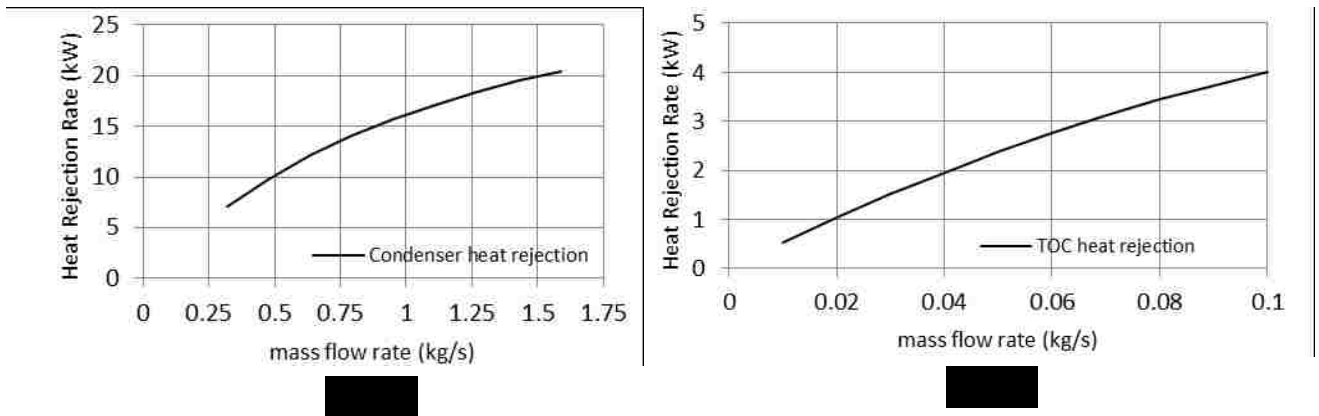


Figure 5.5: Heat rejection as a function of heat exchanger mass flow rate for a) Condenser b) TOC

Figure 5.6 shows the pressure drop characteristics with a pressure drop-velocity graph for the TOC and condenser as obtained from the supplier.

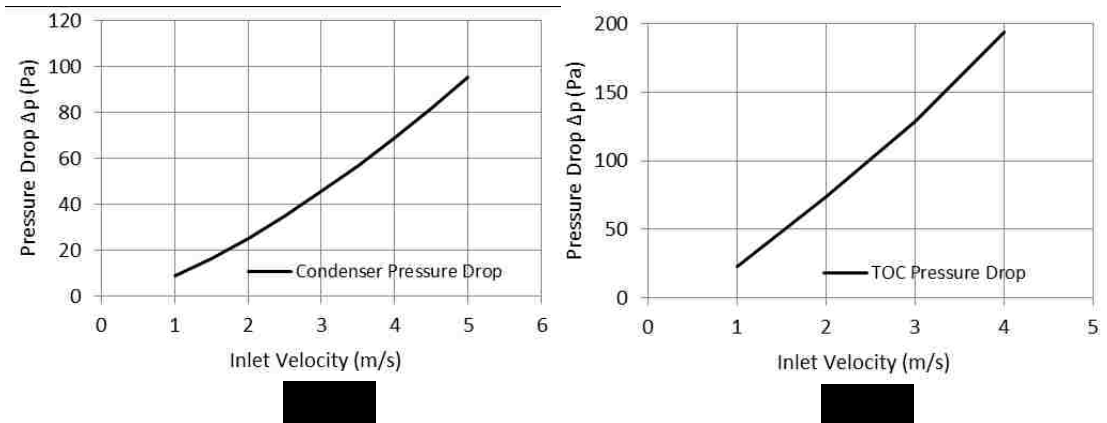


Figure 5.6: Pressure drop as a function of heat exchanger inlet velocity for a) Condenser b) TOC

Details on the supplier data sheets are shown in Appendix B.

Previous results with the radiator modelling in Chapter 4 suggest that pressure drop curves obtained directly from testing require manipulation in order to provide expected results for the different simulation cases. The curves shown above in Figure 5.6 are obtained based on a supplier test for which a tube-side fluid is present, and therefore heat transfer effects are taken into account. Using these curves to represent the heat exchanger pressure drop would, based on experience with the radiator modelling, provide feasible results only for *Case 2*, a simulation for which compressibility effects are neglected and heat transfer effects are included. This curve would provide pressure drops not representative of the iso-thermal *Case 1* and variable density *Case 3* simulations. To quantify these differences, the difference in coefficients and corresponding pressure drops from the radiator modelling will be used as a guideline.

As observed with the isolated radiator modelling, the magnitude of pressure drop across the range of velocities was approximately $\approx 10\%$ higher in *Case 2* (with heat transfer) as compared to the iso-thermal flow conditions. Therefore, the porous media terms obtained from the test curves in Figure 5.6 above for the TOC and condenser will be manipulated to represent this 10% change and new porous terms obtained as inputs into the simulation.

For the variable density simulation, *Case 3*, it was shown that on average, the pressure drop across the range of velocities is approximately $\approx 15\%$ higher in *Case 2* as

compared to the variable density simulations with heat transfer *Case 3*. Once again, new curves are obtained and consequently new porous coefficient terms.

Figure 5.7 summarizes the new curves obtained for each simulation case, while Table 5.2 provides the new porous coefficient terms required as inputs into the simulation that represent the curves shown above. Included in the table are the radiator porous terms as obtained from Chapter 4 as well.

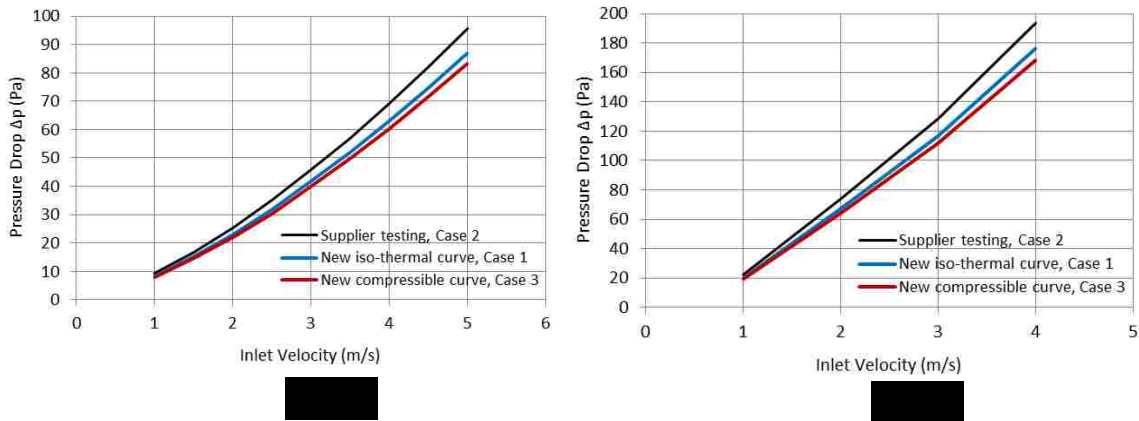


Figure 5.7: Pressure drop as a function of heat exchanger inlet velocity – curve corrections for a) Condenser b) TOC

Condenser			TOC			Radiator		
Case 1	Iso-thermal	Pi = 123 Pv = 483	Case 1	Iso-thermal	Pi = 254 Pv = 832	Case 1	Iso-thermal	Pi = 311 Pv = 456
Case 2	Incompressible with heat transfer	Pi = 135 Pv = 531	Case 2	Incompressible with heat transfer	Pi = 279 Pv = 915	Case 2	Incompressible with heat transfer	Pi = 339 Pv = 506
Case 3	Compressible with heat transfer	Pi = 118 Pv = 462	Case 3	Compressible with heat transfer	Pi = 243 Pv = 796	Case 3	Compressible with heat transfer	Pi = 325 Pv = 336

Table 5.2: Inertial P_i and Viscous P_v porous media resistance coefficient terms for underhood heat exchangers in simulation

Details about the test setup and data collection procedures are not known from the supplier, and therefore no further assumptions or estimates will be made on other pressure losses during the experiment. It is assumed the porous terms in Table 5.2 represent the core-only pressure drop for the TOC and condenser, while assumptions regarding the radiator have been discussed in Chapter 4. This summarizes the inputs

required for each heat exchanger in the CFD simulations, which leaves the fan model as the only major component still to be addressed.

3D modelling of axial fans has made significant advances in the CFD field lately. While different fan modelling techniques are outside the scope of this thesis, some of the techniques are described in the literature review section 2.3. For the fan model, the Moving Reference Frame (MRF) model was adopted, a common technique used in industry. The MRF model is a relatively simple and robust modelling technique of rotating components. It is sometimes referred to as the ‘frozen rotor approach’, because a speed of rotation is assigned to a specific volume (or in some case multiple volumes) in the domain, while the blades themselves are stationary. Therefore, in the user-defined fan domain, a rotating and non-rotating region exist. The flow field can only be observed with the blades at that specific configuration, while additional computations are required if a different orientation of the blades is desired. The fan blades capture the pressure jump and swirl with some degree of accuracy. Errors in this fan model are also discussed in section 2.3. The major advantage of this model is that separate experimental testing is not required; the only input is the rotational velocity, an easily measurable parameter. This steady model approach has proven to provide realistic results for a variety of axial fan modelling in industry. For the simulation input, the fan speed is set to the value obtained from experimental testing Table 5.1, without any optimization or velocity corrections.

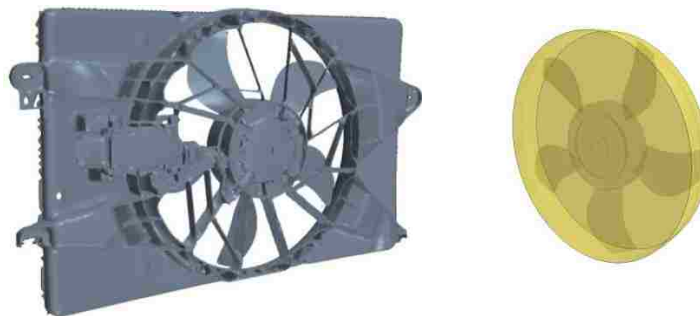


Figure 5.8: a) Fan and shroud geometry b) Fan domain

The last point to include regarding the full vehicle simulation setup is with regards to the different components in the underhood which contain some high surface

temperatures. This would include the exhaust manifold and piping which makes up the rest of the exhaust system. All other components are considered adiabatic. The full vehicle simulation is not developed to predict or update these component temperatures. The assumption is made that convection dominates the underhood airflow, and is the only form of heat transfer accounted for. The component temperatures typically come from experimental testing, or are estimated from previous tests. In experimental testing, the surface temperatures of the exhaust system are generally obtained with thermocouples.

The full vehicle model composed of the sub-models for the different heat exchangers and fan is placed inside a virtual wind tunnel shown in Figure 5.9.

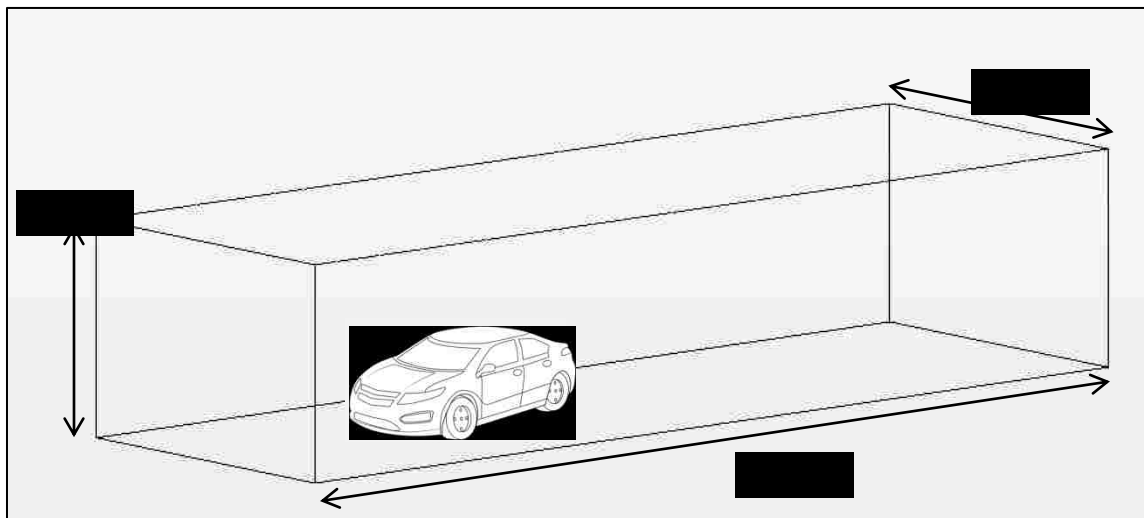


Figure 5.9: Vehicle in representative wind tunnel

The wind tunnel box is modeled with all outside walls smooth, no-slip, and adiabatic except for the wind tunnel floor, which was prescribed a temperature approx. 25 degrees K above ambient air temperature. The front face was prescribed a velocity inlet condition, with the velocity the same as applied in experimental testing. The downstream face was modeled as a pressure outlet boundary condition at ambient pressure and temperature. A hexahedral mesh was once again adopted for the wind tunnel, vehicle and all other components, other than the fan region. The mesh size for each heat exchanger was determined based on the heat exchanger width (depth), where a target of 6-10 cells is considered a best practice and will capture the correct physics [40]. For the fan, a surface

mesh was created in ANSA, and a polyhedral mesh then used in STAR-CCM+ in order to capture the more complex and non-aligned flow around the fan region. This is also reflective of the fan meshing done by [31, 32]. In addition, multiple areas of refinement were used in various vehicle underhood regions, as can be seen in Figures 5.10 and 5.11. The meshing details of each component and regions of refinement are summarized in Table 5.3.

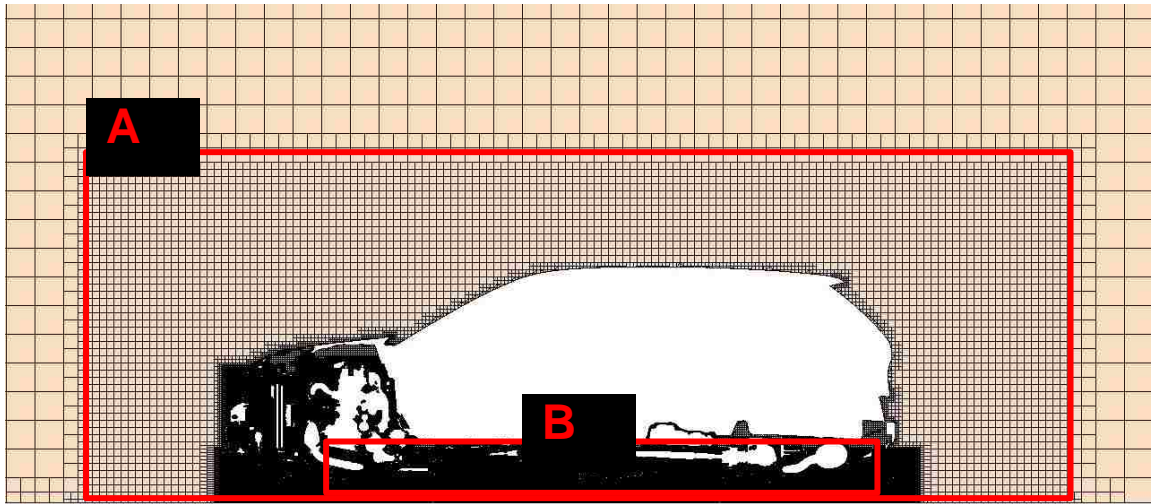


Figure 5.10: Full vehicle and wind tunnel volume mesh in xz-plane

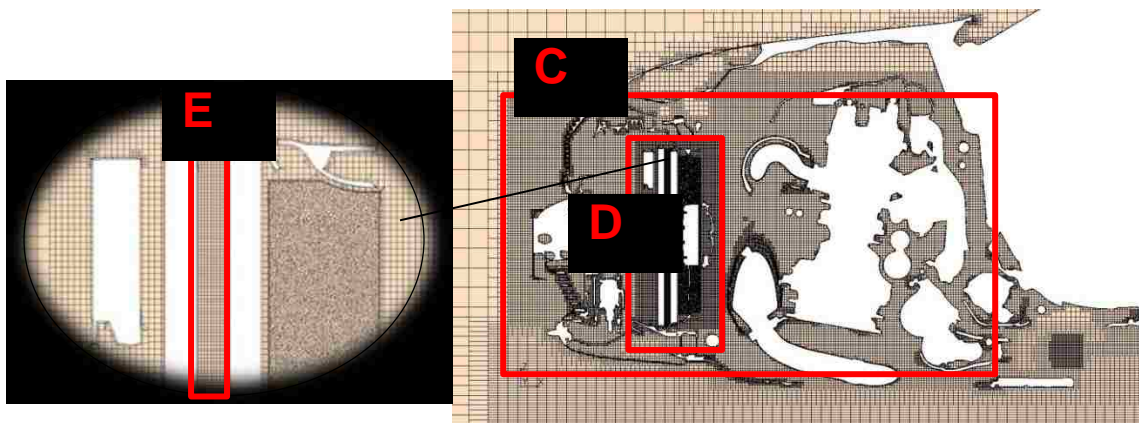


Figure 5.11: Vehicle underhood mesh refinement regions

Refinement region	Mesh base size (mm)	Refinement region	Mesh base size (mm)
Wind tunnel	200	A - vehicle	75
Heat Exchanger volume - TOC, condenser, radiator	10	B - underbody	40 (x), 40(y), 10 (z)
		C - underhood	75
Fan	6	D - heat exchangers	10
		E - condenser downstream/radiator upstream	2.5

Table 5.3: Summary of refinement regions and mesh size allocations

The base size of the vehicle hexahedral mesh was set to 200 mm, which represents the elements seen in the far field wind tunnel region in Figure 5.10. For the fan polyhedral mesh, a base size of 6 mm was used, which can be seen in Figure 5.11. The base size of the heat exchanger cores is 10 mm. These mesh sizes are a result of grid dependence studies performed previously for general underhood simulations. Further mesh studies and mesh adaptation techniques are not performed in this thesis, with the exception of a single “test” mesh, which consisted of a refined base size. This is briefly mentioned in the results section.

To ensure rapid and error-free mesh creation, some pre-processing is required, especially in applying contact prevention settings. Contact prevention ensures that two nearby boundaries or surfaces are not connected unintentionally. The quality of the surface mesh and volume mesh is checked with a mesh diagnosis tool implemented in STAR-CCM+. Thresholds can be assigned for mesh quality parameters such as skewness angle, face validity, cell quality and volume change. The total volume mesh cell count was approximately 31 million cells, comprised of the following component mesh sizes:

Component	Total cell count (thousand)
Wind tunnel and vehicle	26,000
TOC	70
Condenser	310
Radiator (hot and cold core)	370 (x 2)
Coolant tanks	40 (x 2)
Fan	3,500

Table 5.4: Volume mesh cell count

Full vehicle simulations vary slightly with different assumptions and solver settings, but require a time of approximately 60 hours (approx. 2.5 days) on a local machine with 16 processors. Each simulation case is solved until the residuals are converged to less than a normalized value of 10^{-4} , a criteria based on experience with previous underhood simulations and in-line with sources such as [2, 48].

As with the radiator modelling in Chapter 4, a similar procedure of simulation cases was followed with the full vehicle modelling. These cases are summarized below:

Simulation	Description	Equation of State	Porous media coefficients (P _i , P _v)	Fan model
Case 1	Incompressible, iso-thermal	constant density, $\rho = 1.135$	TOC: (254,832) Condenser: (123,483) Radiator: (311,456)	MRF, 2530 rpm
Case 2	Incompressible, with heat transfer	constant density, $\rho = 1.135$	TOC: (279,915) Condenser: (135,531) Radiator: (339,506)	MRF, 2530 rpm
Case 3	Compressible, with heat transfer	ideal gas law, $\rho = P/RT$	TOC: (243,796) Condenser: (118,462) Radiator: (325,336)	MRF, 2530 rpm

Table 5.5: Summary of vehicle simulation cases

The rest of the relevant solver settings are as follows:

- 3D, steady state, Reynolds-Averaged Navier-Stokes equations
- Segregated Flow solver along with the supporting Segregated Fluid Temperature energy model (in the case of heat transfer) with first order discretization schemes
- Realizable k- ϵ two-layer turbulence model, with two-layer all- y^+ wall treatment
- Dual-stream ‘actual’ heat exchanger model for the radiator, ‘heat-source’ heat exchanger model for the TOC and condenser. All heat exchangers modeled as porous media with given porous resistance coefficients in Table 5.5.

The next section will discuss the results of each case described in the above table.

5.4 Results and Discussion

This section will begin with comparing the results of the simulations with experimental testing. After this, the flow and thermal fields at heat exchangers will be evaluated for each simulation case. Note that henceforth, each simulation case will be addressed as per case number;

- *Case 1*: iso-thermal flow conditions (no heat rejection from heat exchangers)
- *Case 2*: incompressible hot flow condition (with heat transfer effects)
- *Case 3*: variable density hot flow conditions (with heat transfer effects)

Before the results are shown, an important note regarding the validation procedure is addressed. The only parameter that is available to compare with experimental testing in this study is the radiator water-side temperature change, and consequently the heat transfer rate, which is assumed to be consistent for the two fluids. This leaves no method to explicitly validate the *Case 1* simulation, since no hot fluid mass flow rate is prescribed. In essence, when comparing the hot fluid temperature change in the simulations with experimental testing, the results reflect the accuracy of the iso-thermal simulation as well as the accuracy with which the modelling techniques of the TOC, condenser and fan are implemented. It is undeniably a large dependency to put upon one measured parameter, but is a recognized limitation in this thesis regarding the availability of experimental data for validation purposes.

Table 5.6 shows the heat rejection and water-side temperature predictions for simulation *Case 2* and *Case 3* as compared to experimental testing.

	Radiator water-side ΔT (K)	Error	Radiator air-side ΔT (K)	Heat rejection rate (W)
Full Vehicle Experiment	9.5	-	-	35255
Full Vehicle Case 2	8.5	10%	34.7	31273
Full Vehicle Case 3	8.0	16%	34.1	29536

Table 5.6: Full vehicle experimental testing and simulation results

Recall that for the radiator, the hot inlet temperature was a specified boundary condition, and the heat rejection rate is a predicted quantity, as outlined in the dual-stream heat exchanger model in section 3.6. From the results above it can be seen that both simulations with heat transfer *Case 2* and *Case 3* represent the water-side temperature decrease reasonably well. The difference in air temperature is large however, but since measurements of this parameter are not available, not much can be said regarding the air temperature accuracy. It should be noted that a 1°C decrease in water temperature results in a 3-4°C increase of air, and that estimating airside temperatures (or mass flow) from experimental testing would be beneficial for validation of such studies. As is often the case in heat exchangers, the airside flow is often the “limiting” fluid, and additional results may provide further insight into the discrepancies in Table 5.6. The next few pages will provide further insight into parameters such as temperature and mass flow rate at different heat exchanger interfaces for all three simulation cases; iso-thermal *Case 1*, constant density with heat transfer *Case 2*, and variable density with heat transfer *Case 3*.

Full vehicle simulations early in the vehicle development cycle are frequently performed under iso-thermal conditions. The reason for this has been mentioned before, and is mainly due to the fact that information such as cooling module performance and component packaging is not available. Therefore, it will be of interest to compare the *Case 1* flow field conditions with the other two simulation cases of heat transfer.

Of particular interest is the mass flow rate at the inlet face of the radiator for reasons mentioned previously. This mass flow rate will directly impact the radiator performance, which is established through the *Qmap* table. The mass flow rate is an input to the table, with the output being the heat rejection rate and therefore a water-side temperature change of some magnitude, as shown in Table 5.6. This analysis would not be possible if the radiator was treated as a volumetric heat source in the simulations, such as the model used with the condenser and TOC. This also partially explains why the radiator modelling has been a dominant topic in this thesis.

The modelling techniques adopted for the rest of the cooling modules will also impact this mass flow rate, and therefore their influence needs to be captured. The simplified

models used for the other cooling modules may raise some questions. For example, the volumetric heat source adopted for the TOC and condenser heat exchangers may not capture the temperature distribution correctly, as it is assumed that each cell in the region has a uniform temperature and removes/adds a specified amount of heat flow. This would of course not be the case if a cross-flow hot stream was introduced. Also, the MRF fan model brings up several issues and errors, most of which have been mentioned previously and will be noted again at the end of this section. While discrepancies may exist with the use of these simplified models, the goal of absolute accuracy is not required here, as is often the case early in vehicle development programs. Also, any discrepancies would be consistent for each simulation case.

Figure 5.12 shows the mass flux distribution at the front face of the radiator for each of the three cases, see Table 5.5 for details.

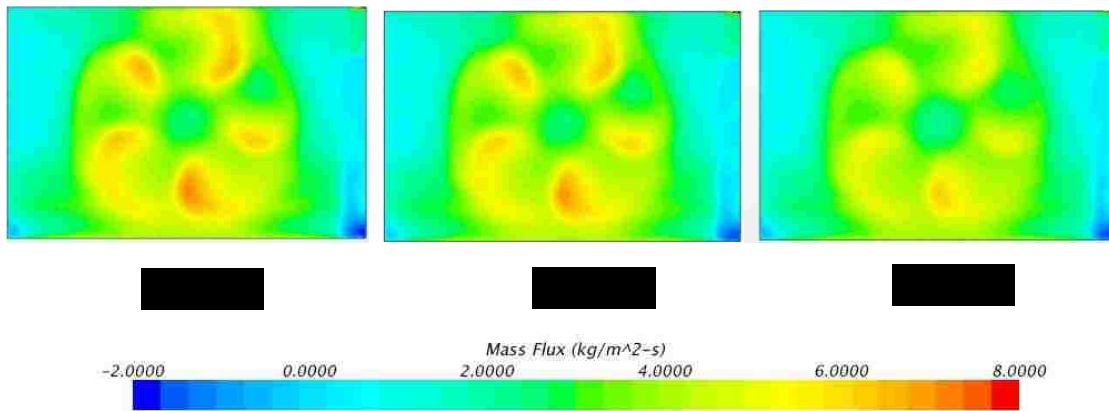


Figure 5.12: Mass flux distribution at radiator inlet for each simulation

There is a clear trend towards a lower overall mass flow rate from *Case 1* to *Case 3*, which would suggest that heat transfer effects and compressibility effects predict a lower mass flow rate than what is seen in an incompressible iso-thermal simulation *Case 1*. What is also evident is the presence of the fan blades projection on the radiator core, an effect not reflective of what is observed in a real situation. In the blade “area”, the highest mass flow rate is observed. This suggests that the fan blade ‘frozen’ position must have an effect on the fan performance and therefore the mass flow rate recognized at the radiator inlet. In addition, this fan has five blades, which would present questions regarding the influence of the fan geometry on the performance of the MRF modelling

technique, as different geometries and number of blades would surely produce a different flow field. Fan analysis is outside the scope of this thesis, but a small section in Chapter 7 is dedicated to comments regarding future work on fan effects.

Mass flow rate values at the radiator inlet face are reported in Table 5.7, along with other parameters of interest for each simulation case. A reminder that the only input parameter adjusted, apart from compressibility and heat transfer effects, is the porous media coefficient terms to represent the trend as observed in Chapter 4 regarding radiator pressure drop values for each simulation case.

	Mass flow rate (kg/s)	Air inlet temperature (K)	inlet density (kg/m ³)	Air pressure drop (Pa)	Face velocity (m/s) <i>i-direction</i>
Case 1	0.911	311.2	1.135*	68.73	2.74
Case 2	0.896	329.6	1.135*	72.75	2.70
Case 3	0.823	330.1	1.066	70.85	2.63

Table 5.7: Relevant radiator results for each simulation case

These results suggest that performing a full vehicle simulation under the consideration of *Case 1* conditions, the mass flow rate through the radiator is 1.6% larger as compared to *Case 2*, and 9.6% larger when compared to *Case 3*. The latter percentage difference is somewhat of an unexpected result. The next few pages discuss the differences observed in Table 5.7 and attempt to provide reasoning for some of the differences.

The lower face velocity for *Case 3* as compared to the other two cases is an unexpected outcome. This is because the law of conservation of mass must be realized in each heat exchanger, and thus with a change in density due to heat transfer, it is expected that the velocity must increase to satisfy this law. This was shown to be the case in the variable density simulations performed in Chapter 4 with the radiator, where a velocity increase between inlet and outlet interfaces was as high as 9%. If vehicle upstream conditions are consistent, the TOC and condenser should reflect a velocity increase through their respective cores and result in a velocity at the radiator face which is higher in *Case 3* than the other simulation cases. The lower mass flow rate observed in *Case 3* is therefore a result of a lower face velocity ($\approx 4\%$) and a density change ($\approx 6\%$).

Furthermore, it is interesting to note that despite the lower porous media terms adopted for the *Case 3* (see Table 5.2), the observed face velocity and corresponding 12% velocity increase (not shown above) through the radiator core is not enough to match the *Case 2* pressure drop. Ensuring that *Case 2* and *Case 3* pressure drop values were similar was the original intention when assigning a “correction” of the porous coefficient curve in Figure 4.15. However, this difference in pressure drop is very minimal, which brings up another interesting observation. From the isolated radiator testing and simulations in Chapter 4, it was shown that with heat transfer taken into account (as opposed to “cold” conditions), the radiator core pressure drop increased by $\approx 10\%$. This increase in a full vehicle underhood simulation is about half; $\approx 5\%$ increase from “cold” *Case 1* to “hot” *Case 2* as shown in Table 5.7.

Changes in mass flow rate at the radiator would suggest changes in the upstream flow field as well. Therefore, evaluating similar parameters at the TOC and condenser can provide further insight into what is causing these differences. Figures 5.13 and 5.14 show the mass flux distribution, while Tables 5.8 and 5.9 provide similar data, for the TOC and condenser, respectively.

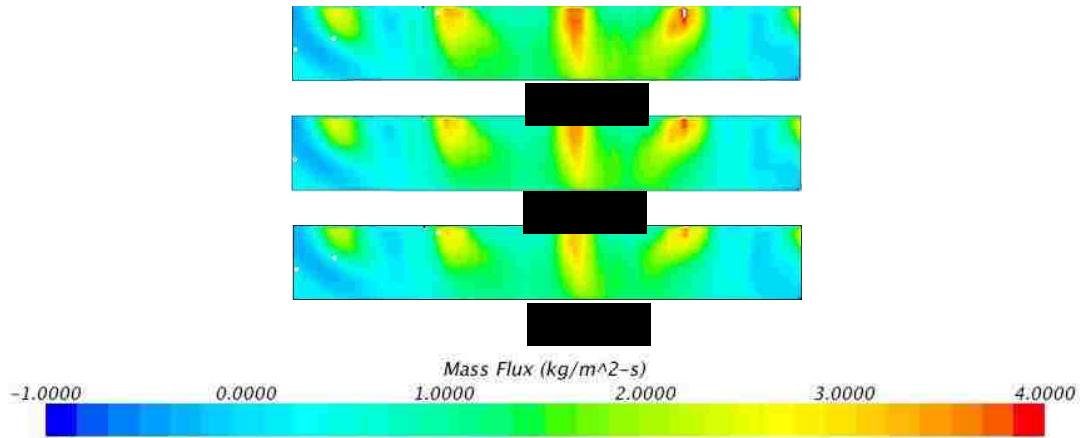


Figure 5.13: Mass flux distribution at TOC inlet for each simulation case

	Mass flow rate (kg/s)	Air inlet temperature (K)	inlet density (kg/m ³)	Air pressure drop (Pa)	Face velocity (m/s) <i>i-direction</i>
Case 1	0.050	311.2	1.135*	29.54	1.04
Case 2	0.047	312.5	1.135*	29.31	0.98
Case 3	0.041	312.6	1.126	24.34	0.86

Table 5.8: Relevant TOC results for each simulation case

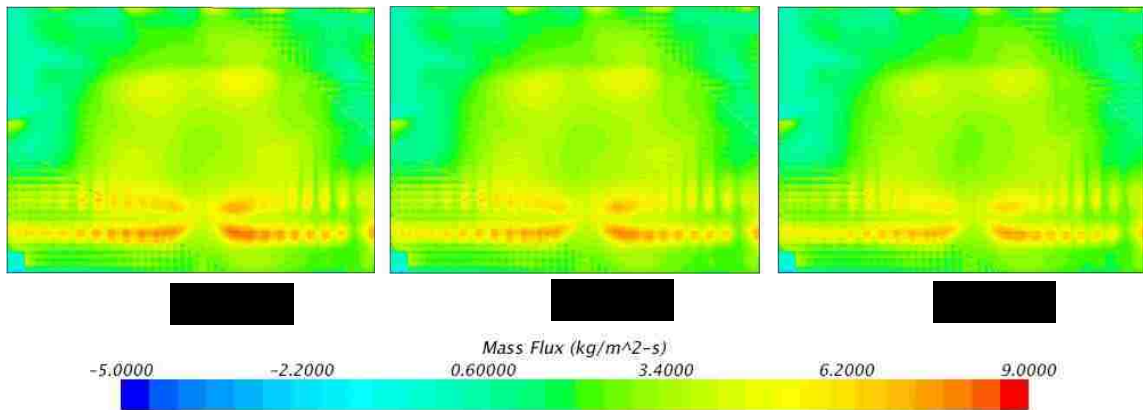


Figure 5.14: Mass flux distribution at condenser inlet for each simulation

	Mass flow rate (kg/s)	Air inlet temperature (K)	inlet density (kg/m ³)	Air pressure drop (Pa)	Face velocity (m/s) <i>i-direction</i>
Case 1	0.860	311.2	1.135*	39.01	2.73
Case 2	0.844	314.1	1.135*	41.28	2.68
Case 3	0.778	314.1	1.121	34.52	2.50

Table 5.9: Relevant condenser results for each simulation case

The mass flux distribution seen on the TOC inlet is due to the upper grille geometry, which consists of several vertical openings equally spaced apart. This results in a pattern of low and high gradients as seen in Figure 5.13. For the condenser, the higher mass flow rate towards the bottom third of the frontal area is due to the lower grille opening. In addition, the fan contour is clearly visible, although less pronounced in *Case 3*. This would suggest that fan effects also change under different flow assumptions, such as heat transfer and compressibility. Additionally, at the condenser face, the obstruction of the TOC is also distinguishable.

It is evident that with the TOC and condenser, a similar trend is present as seen at the radiator inlet with regards to mass flow rate. That is, a lower mass flow rate is present in *Case 2* and in *Case 3* relative to *Case 1*. Since this is observed also at the TOC inlet and affects all downstream heat exchangers, this would suggest the possibility of less mass flow rate entering the underhood compartment under heat transfer and compressibility effects, and maybe diverted to other areas of the vehicle. However, it is difficult to analyze where this occurs in the domain. An attempt to support this hypothesis is shown in Figure 5.15. The images show the mass flux distribution of the vehicle underhood in the longitudinal plane. In STAR-CCM+, it is not possible to directly plot mass flow rate or mass flux distribution at derived (user-defined) section planes. This is because the mass flow is displayed on cell faces, while derived surfaces cut directly through cells. Therefore, the mass flux value shown here is based on a user-defined function which consists of simply the density multiplied by the *i*-component of velocity. This approach is verified by comparing the mass flux distribution at a boundary condition, and produces similar results as using the built-in mass flux report.

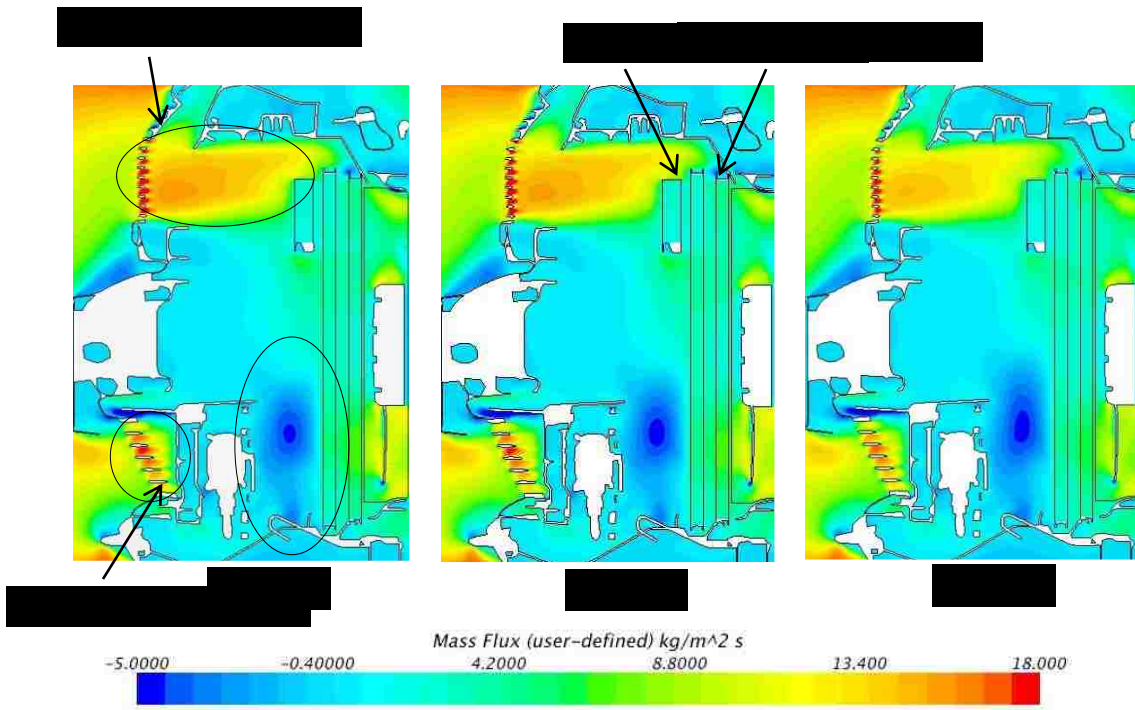
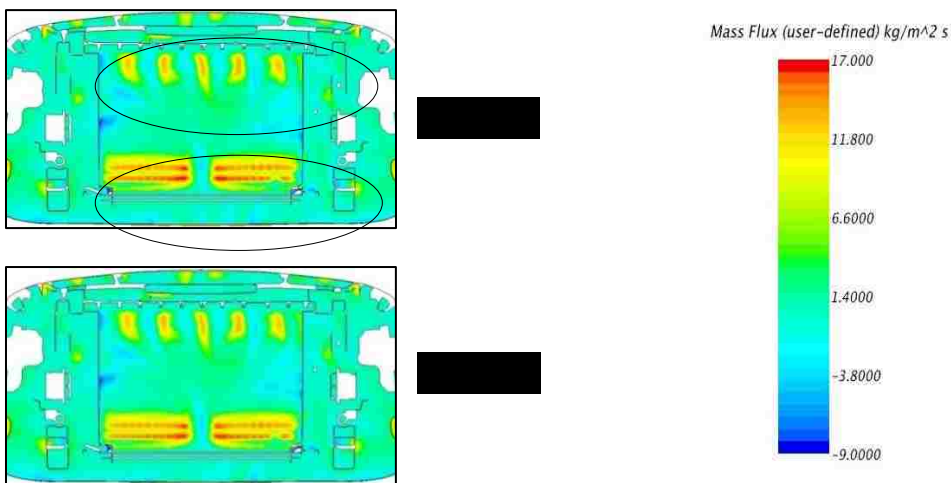


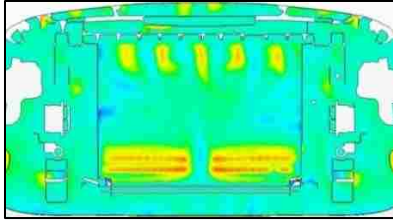
Figure 5.15: Mass flux distribution in vehicle underhood

The main regions of focus are downstream of the upper grille and at the lower grille, as outlined in the image of *Case 1*. In addition, a re-circulating region is present upstream of the condenser, and a region of higher mass flow rate at the fan blade.

In the region downstream of the upper grille, the difference is most pronounced in *Case 3*, where lower values are clearly present. This will have the greatest influence on the mass flow rate at the TOC. Furthermore, although perhaps not as evident, is at the lower grille, which will have a greater impact on the mass flow at the condenser inlet face. The region of re-circulation just upstream of the condenser, as evident by the darker blue shade encircled above, is most prominent in *Case 3* and likewise affects mostly condenser flow. The circled region at the fan blade would suggest again that fan effects vary with different flow assumptions.

Overall, these somewhat distinguishable regions should account for the majority of the contribution in the numerical differences observed in Tables 5.7, 5.8 and 5.9 for the mass flow. From Table 5.8 for the TOC, the mass flow rate represents a decrease of 6% in *Case 2* and 18% in *Case 3*, relative to *Case 1*. For the condenser from Table 5.9, the decrease is 2% in *Case 2* and 10% in *Case 3* relative to *Case 1*. Furthermore, a decrease in density in *Case 3* will contribute to an even lower mass flow rate at each heat exchanger. In support of Figure 5.15, a transverse plane slightly upstream of the TOC is shown of the underhood in the Figure below, for each simulation case. A similar trend exists here; a stronger gradient especially at the upper and lower grille openings for *Case 1*, as compared to *Case 2* and more significantly, *Case 3*.





Regarding air temperature values, it is observed that the temperature distribution and overall temperature increase of the air is little changed between the simulation cases upstream of the radiator. It is true that with a slightly lower mass flow rate in the TOC and condenser, a lower overall heat source term will be applied as per the look-up tables mentioned in section 5.3. The user-defined tables (obtained from data sheets) are not overly sensitive; a change in mass flow rate of $\pm 10\%$ is still very low in absolute magnitude to result in major increase/decrease of heat rejection rates and consequently, large air temperature differences. In fact, the air inlet temperatures are almost identical at each heat exchanger between the two simulation cases, as shown in Table 5.10. The air temperature change through the radiator is also very similar, and is mainly due to the fact that despite the lower heat rejection in *Case 3*, the lower mass flow rate ends up with air temperature increases of similar magnitude as compared to *Case 2*, where a larger mass flow rate, but also a slightly higher heat rejection, is present. Table 5.10 provides an overall summary of each simulation case and the relevant parameters of interest. All values, except for the coolant inlet temperature are output values as calculated by the software.

	TOC				Condenser				Radiator					
	Air mass flow (kg/s)	Heat rejection (kW)	Air temp inlet (K)	Air temp outlet (K)	Air mass flow (kg/s)	Heat rejection (W)	Air temp inlet (K)	Air temp outlet (K)	Air mass flow (kg/s)	Heat rejection (W)	Air temp inlet (K)	Air temp outlet (K)	Coolant temp inlet (K)	Coolant temp outlet (K)
Case 1	0.050	-	311.1	311.1	0.86	-	311.2	311.2	0.911	-	311.2	311.3	-	-
Case 2	0.047	2.24	312.5	354.8	0.84	14.62	314.1	330.9	0.896	31.27	329.6	364.3	379	370.5
Case 3	0.041	2.01	312.6	355.4	0.78	14.00	314.2	331.3	0.823	29.53	330.1	364.2	379	371.0

Table 5.10: Heat rejection rates and temperatures for each heat exchanger

In an attempt to disprove, or otherwise provide further confidence in the results discussed so far, several arguments can be made and are considered here before a conclusion is provided to this chapter.

The initial idea was that a criterion of 10^{-3} for convergence in the continuity residual is not enough to guarantee small fluctuations in the mass flow do not occur in the domain. However, despite the residual reaching an absolute value of 10^{-8} or less for each simulation case, small differences in the range of hundredths or thousandths of a decimal still exist. An example to provide further clarity, one sectional plane downstream of the vehicle shows a mass flow rate that is 0.0001% higher than a similar (in area) sectional plane upstream of the vehicle. This is equivalent to approximately a 0.02 kg/s change, which is negligible on a global scale. Locally however, such as at the TOC inlet, this can contribute to an almost 50% increase in mass flow! The author is therefore reluctant to disregard these differences as having an effect on the recorded values of flow in Table 5.10, despite each simulation case displaying identical trends. Additionally, when reporting total mass flow rate over arbitrary sectional planes in the domain, there is an unknown error associated with the interpolation of the cell faces to report this value.

To confirm trends observed thus far regarding mass flow rate, additional simulation tests can be performed, perhaps under simpler geometries and less components. For example, a first step could be to neglect a rotating fan. Much of the discussion on fan performance has been avoided, but it is important to note that the fan influence on the flow under heat transfer and compressibility effects has not been studied or evaluated in this research. It is uncertain how the simplified fan model applied in this study may be affected by these types of flows. The images shown earlier regarding mass flux distribution at the condenser and radiator would suggest that different assumptions affect fan performance, and could adversely affect mass flow rate at each heat exchanger.

The simulation cases were performed with a finer mesh as well. As mentioned, mesh studies were not conducted; simply a test simulation to observe effects of decreased mesh size was performed. The base size was decreased to 150 mm, a reduction of 25%. This resulted in nearly double the computational time required to reach convergence. No changes could be reported for any parameters of interest. Boundary conditions were also manipulated for the simulation *Case 3*, in which total conditions (pressure, temperature) were specified at the inlet, and a negative velocity inlet was prescribed at the outlet boundary. This would allow for an easier solution to the flow field, and is perhaps

confirmed by the small reduction in computational time ($\approx 15\%$) for the simulation case with variable density with no changes in the results.

A final comment regarding mass flow rate is related to the earlier suggestion of flow diversion which may result in lower mass flow rates at the heat exchangers. Buoyancy effects were not thoroughly explored for each simulation case, but are expected to have a negligible effect at underhood flow velocities of this magnitude. It was also not possible to identify visualization plots or provide reports which account for higher mass flow rates being diverted to other regions of the underhood, or even around the vehicle. This brings this chapter to a close, which seems to end with more questions and ideas than concrete conclusions.

Based *only* on the simulation results obtained, it is observed that vehicle underhood simulations performed under constant density iso-thermal conditions may over-estimate the mass airflow at the radiator; by approximately 2% as compared to a simulation case under constant density including heat transfer effects, and by approximately 10% when performing a simulation with a variable density and including heat transfer effects. The small 2% difference is well within generally acceptable limits of error and would suggest that heat transfer effects do not have a large impact. But it should be noted that the correct velocity field through the heat exchangers is not captured in constant density simulations, as occurs in a real underhood scenario. Naturally, these conclusions contain several simplifications and effects which need to be considered and further investigated in order to provide confidence in the results.

6. CONCLUSIONS

The research in this thesis was focused on exploring modelling techniques for vehicle underhood simulations and investigating the effects of heat transfer and compressibility on the cooling airflow. Specific conclusions have been formed at the end of Chapter 4 and Chapter 5, which are summarized as follows:

- It was shown that predicting airflow behaviour through an isolated radiator case with no heat transfer is possible with a porous media approach, with small error in prediction at lower flow rates. This is simply due to the approximation of pressure drop with a second order polynomial. In addition, for this specific test facility, pressure losses upstream and downstream of the radiator core are present and need to be accounted for in order to correctly estimate the core-only pressure drop.
- Introducing a water-side (hot) stream, it is possible to obtain a good correlation with experimental results for the air and waterside parameters using a dual-stream heat exchanger model in the constant density simulations. That is, by applying the pressure drop-velocity curves obtained from experimental testing to a constant density simulation, the approx. 10% increase in pressure drop due to heat transfer is correctly predicted. When considering the effects of variable density, the curve representing the pressure drop needs to be corrected or adjusted in order to avoid accounting for the heat transfer effects on thermo physical properties twice. The correction required in this study was approx. a 15% decrease in pressure drop. By applying this correction, airside and waterside thermal properties remain unchanged, and pressure drop values show a good correlation with experimental data.

Upstream and downstream pressure losses are still present and similar in magnitude as obtained with the iso-thermal simulation, recorded in Table 4.5.

- An analysis of a full underhood compartment requires several additional models and assumptions. Similar corrections and differences observed in radiator pressure drop curves for each simulation case are applied to the other

two heat exchangers present; in this case, the pressure drop curves of a transmission oil cooler and condenser. This results in a pair of porous terms for each heat exchanger for each simulation scenario (three in total). A simplified Moving Reference Frame (MRF) approach is used to model the fan without any additional fan validation or correction methods.

For the simulations with heat transfer, this approach predicted experimental results of coolant temperature change within a reasonable range, under-predicting the change in coolant temperature by 1°C for constant density simulation (*Case 2*), and by 1.5°C for variable density (*Case 3*).

- It was observed that radiator mass flow rate varied with each simulation. Out of the three simulation cases adopted in this study, the incompressible isothermal simulation referred to as *Case 1* produces the largest total mass flow at the radiator. Using this as a reference, *Case 1* tends to over-estimate mass flow rates by 2% for a constant density simulation with heat transfer, and 10% for a variable density simulation with transfer effects. These reported mass flow rate figures however contain several unexplored effects that were outside the scope of this thesis and potential errors that were not identified in this study, but should be considered for future studies and simulations.

7. RECOMMENDATIONS FOR FUTURE WORK

Performing 3D CFD simulations of an isolated heat exchanger and a full vehicle underhood compartment has provided valuable insight into the challenges faced in the development of vehicle thermal management systems. Several opportunities exist for improvements that can be implemented in order to provide further confidence in the results obtained in this study, both from an experimental perspective and in vehicle virtual modelling. Some recommendations for future work are as follows:

- In Chapter 4, pressure losses upstream and downstream of the heat exchanger core were investigated to obtain a better estimate of the core-only pressure drop. For a more accurate estimate of this figure, the test setup can be improved with the addition of a bell-mouth duct upstream of the mounted heat exchanger core. This has been implemented in several experimental tests in other research as well, and has shown to significantly reduce the total pressure losses upstream.
- Velocity/mass flow and/or temperature measurements at the heat exchanger would provide additional data for validation of the simulation results. Hot-wire velocity probes can be placed in the heat exchanger core or cylindrical pressure probes upstream and downstream of the core for mass flow rate measurements, as mentioned in [30]. However, the number of probes must be considered thoroughly, in order to reduce a higher pressure loss due to the probes themselves but still provide a good resolution. This impact can be measured on a stand-alone test bench, and taken into consideration if implemented in more complex geometries, such as in a full vehicle. For temperature distribution at the heat exchanger, further investigations into placement of thermocouple probes in the heat exchanger core would also provide useful data for validation.

If sensors can be accurately implemented in the full vehicle simulation, it can eliminate one of the greatest limitations in this study, which is the lack of experimental test data for validating the full vehicle simulation cases.

Towards the end of this study, some airside flow data became available, but due to time constraints, was not thoroughly explored and used in this thesis. The first step would be to use this data or perform further experimental tests to be able to validate the full vehicle iso-thermal simulation.

- It has been shown that porous media models can be used to accurately implement the pressure drop across the heat exchangers, except at lower mass flow rates. A significant error is observed at lower velocities, which is due to the approximation of pressure drop in a porous media by a second order polynomial, with an intercept at $(0,0)$. This forced interception point is not an ideal representation of the pressure drop at low flows, and tends to increase in error as velocity tends to zero. Instead, a second order polynomial with a constant would provide a better correlation, or perhaps pressure drop at low flows can be described with a different trend line. Unfortunately, most CFD codes use this standard two-coefficient porous media approach.
- The impact of the TOC was initially assumed to be minimal, due to its relatively low frontal area. However, it was observed that the air temperature increase across the TOC core is significant, and can impact the flow in the downstream components, such as the condenser and radiator. To improve the overall accuracy of the airflow in the underhood compartment, a dual-stream heat exchanger can be adopted for the TOC heat exchanger as well. This would provide more realistic results, especially with respect to the temperature distribution. In addition, an increase in computational demand by adding another hot stream may be insignificant, due to the fact it is not very large and will therefore not result in a large increase in cell count.
- For an accurate prediction of the underhood cooling airflow, the fan is a necessary component to include as it is one of the main drivers of cooling airflow. Accurate fan modelling continues to be a real challenge for underhood CFD simulations. In this study, the fan is perhaps the most inaccurate component. Despite it not being a main part of the study, it would be foolish not to acknowledge the inaccuracies due to the fan model. For this study, the Moving Reference Frame (MRF) fan model is adopted. Several

recommendations are made without getting into too much detail. Due to its relative simplicity and the fact that it does not rely on any measurements, it is a widely adopted approach in industry. However, MRF model is known to under-predict the pressure rise across the fan, and therefore also under-predict the airflow drawn into the heat exchangers. In addition, it works under the assumption of stationary flow, which according to [33], implies that the stationary geometry close to the fan needs to be rotationally symmetric, an impossible constraint in a vehicle underhood. In order to account for this under-prediction, a simple fan speed correction is suggested, in order to predict a cruising condition most accurately, while under-prediction still exists at full fan operating condition. As an example, for a 750 mm fan, this correction was a 14% increase in fan speed.

The fan blockage is clearly visible at the condenser and radiator inlet faces, as shown in section 5.3. Higher mass flow can be observed in the blade passage, and while this is in fact reflective of the real fan physics, it is also true that in a real situation the fan blades rotate. Therefore, the mass flow rate and velocity peaks are significantly lower. It is therefore important to observe the MRF model under different position of fan blades. By rotating the fan, it is possible to obtain and plot an average distribution of each position, which is more reflective of a real transient fan model.

It is suggested however, that fan testing also be performed before any changes and conclusions are made from the simulations. Fan testing with this exact fan model can provide a general correction method for future applications using similar fans. It is important to investigate non-symmetrical blockage effects, by perhaps testing the stand-alone fan with 3D mock-ups of the upstream and downstream geometry, also used in [31, 33]. In addition, as was mentioned at the end of Chapter 5, effects of heat transfer and compressibility on the fan MRF model are unknown, and should be investigated in order to ensure that reported mass flow rates are not significantly impacted by different flow assumptions.

Much of the discussion and suggestions for the fan modelling is based on previous work by Gullberg [31-35], and referenced several times throughout this thesis.

- Further investigation into the impact of the wind tunnel floor boundary condition, which was prescribed a surface temperature, and not treated as an adiabatic wall (such as was the case with the other walls). The impact of this temperature on the upstream (of the vehicle) boundary layer may influence the mass flow rate at the vehicle grille.
- Further investigation into the uncertainties of the experimental tests performed on the isolated radiator and in the full vehicle wind tunnel, would provide further insight into the accuracy of tests and correlation with simulation results.
- Regarding the full vehicle simulations, if external and underbody flow are not of interest, pursuing a half-vehicle model can be advantageous due to the significant reduction in element count. The half-vehicle model is still relatively simple to implement and may not require solving any boundary conditions before-hand. However, the limitation is that a symmetrical domain is required to perform these simulations with accuracy.

REFERENCES

- [1] Retrieved November 13, 2016, from <http://www.epa.gov/emissions>
- [2] Regin, F., Agarwal, A., & Mishra, N. K. (2014). Passenger car front end optimization using CFD simulation. *SAE Technical Paper Series*. doi:10.4271/2014-01-0627
- [3] Lu, P., Gao, Q., & Wang, Y. (2016). The simulation methods based on 1D/3D collaborative computing for the vehicle integrated thermal management. *Applied Thermal Engineering*, 104, 42-53. doi:10.1016/j.applthermaleng.2016.05.047
- [4] Wang, G., Gao, Q., Zhang, T., & Wang, Y. (2016). A simulation approach of under-hood thermal management. *Advances in Engineering Software*, 100, 43-52. doi:10.1016/j.advengsoft.2016.06.010
- [5] Carbon Emissions Report. Retrieved October 20, 2016, from <https://ourworld.unu.edu/en/reports>
- [6] Khaled, M., Harambat, F., & Peerhossaini, H. (2010). Temperature and heat flux behavior of complex flows in car underhood compartment. *Heat Transfer Engineering*, 31(13), 1057-1067. doi:10.1080/01457631003640321
- [7] Kim, H. J., & Kim, C. (2008). A numerical analysis for the cooling module related to automobile air-conditioning system. *Applied Thermal Engineering*, 28(14-15), 1896-1905. doi:10.1016/j.applthermaleng.2007.12.002
- [8] Singh, R., & Shen, F. (2007). CFD-based robust optimization of front-end cooling airflow. *SAE Technical Paper Series*. doi:10.4271/2007-01-0105
- [9] Bayraktar, I. (2012). Computational simulation methods for vehicle thermal management. *Applied Thermal Engineering*, 36, 325-329. doi:10.1016/j.applthermaleng.2011.10.040
- [10] Melzer, F., Hesse, U., Rocklage, G., & Schmitt, M. (1999). Thermomanagement. *SAE Technical Paper Series*. doi:10.4271/1999-01-0238
- [11] Mahmoud, K. G., Loibner, E., Wiesler, B., Samhaber, C., & Kußmann, C. (2003). Simulation-based vehicle thermal management system - concept and methodology. *SAE Technical Paper Series*. doi:10.4271/2003-01-0276
- [12] Mahmoud, K. G., Loibner, E., & Krammer, J. (2004). Integrated 1-D tools for modeling vehicle thermal management system. *SAE Technical Paper Series*. doi:10.4271/2004-01-3406

- [13] Fortunato, F., Damiano, F., Matteo, L. D., & Oliva, P. (2005). Underhood cooling simulation for development of new vehicles. *SAE Technical Paper Series*. doi:10.4271/2005-01-2046
- [14] Alajbegovic, A., Sengupta, R., & Jansen, W. (2006). Cooling airflow simulation for passenger cars using detailed underhood geometry. *SAE Technical Paper Series*. doi:10.4271/2006-01-3478
- [15] Chen, S., & Doolen, D.G. (1998). Lattice Boltzmann method for fluid flows. *Annual Review of Fluid Mechanics*. 30:329-364
- [16] Yeomans, J. M. (2002). The Lattice Boltzmann equation for fluid dynamics and beyond, Sauro Succi Princeton U. Press, New York, 2001. ISBN 0-19-850398-9. *Physics Today*, 55(12). doi:10.1063/1.1537916
- [17] Juan, T. (2008). Investigation and assessment of factors affecting the underhood cooling air flow using CFD. *SAE Technical Paper Series*. doi:10.4271/2008-01-2658
- [18] Khaled, M., Alshaer, A., Hachem, F., Harambat, F., & Peerhossaini, H. (2012). Effects of ground vehicle inclination on underhood compartment cooling. *International Journal of Automotive Technology*, 13(6), 895-904. doi:10.1007/s12239-012-0090-8
- [19] Jama, H., Watkins, S., Dixon, C., & Ng, E. (2004). Airflow distribution through the radiator of a typical Australian passenger car. *15th Australasian Fluid Mechanics Conference*, Sydney, Australia.
- [20] Uhl, B., Brotz, F., Fauser, J., & Krüger, U. (2001). Development of engine cooling systems by coupling CFD simulation and heat exchanger analysis programs. *SAE Technical Paper Series*. doi:10.4271/2001-01-1695
- [21] Khaled, M., Ramadan, M., El-Hage, H., Elmarakbi, A., Harambat, F., & Peerhossaini, H. (2014). Review of underhood aerothermal management: Towards vehicle simplified models. *Applied Thermal Engineering*, 73(1), 842-858. doi:10.1016/j.applthermaleng.2014.08.037
- [22] Alajbegovic, A., Xu, B., Konstantinov, A., Amodeo, J., & Jansen, W. (2007). Simulation of cooling airflow under different driving conditions. *SAE Technical Paper Series*. doi:10.4271/2007-01-0766
- [23] Salvio, C., Biswadip, S., Vinod, K., Agarwal, K., & Katkar, D.R., (2003) Numerical simulation for improving radiator efficiency by air flow optimization. *Engineering Research Center of Tata Motor Limited India*.
- [24] Knaus, H., Ottosson, C., Brotz, F., & Kühnel, W. (2005). Cooling module performance investigation by means of underhood simulation. *SAE Technical Paper Series*. doi:10.4271/2005-01-2013
- [25] Seider, G., Bet, F., Heid, T., Hess, U., Klein, T., & Sauer, J. (2001). A numerical simulation strategy for complex automotive cooling systems. *SAE Technical Paper Series*. doi:10.4271/2001-01-1722

- [26] Jerhamre, A., & Jönson, A. (2004). Development and validation of coolant temperature and cooling air flow cfd simulations at volvo cars. *SAE Technical Paper Series*. doi:10.4271/2004-01-0051
- [27] Yang, Z., Bozeman, J., & Shen, F. Z. (2004). CFD for flow rate and air re-circulation at vehicle idle conditions. *SAE Technical Paper Series*. doi:10.4271/2004-01-0053
- [28] Jones, M. R., & Fletcher, D. W. (2001). Thermal performance prediction of front-end heat-exchange modules. *SAE Technical Paper Series*. doi:10.4271/2001-01-1765
- [29] Skea, A., Jolliffe, A., Harrison, R., Jones, M., Cardani, P., & Smith, L. (2002). Underbonnet thermal management prediction. *4th Vehicle Aerodynamics Conference, Mira International, Warwick, UK*.
- [30] Wille, S., Kuthada, T., Widdecke, N., Wiedemann, J., Maier, H., & Koller, A. (2010). Integrated numerical and experimental approach to determine the cooling air mass flow in different vehicle development stages. *SAE International Journal of Passenger Cars - Mechanical Systems*, 3(1), 352-365. doi:10.4271/2010-01-0287
- [31] Gullberg, P. (2011). Optimisation of the flow process in engine bays - 3d modelling of cooling airflow. *Department of Applied Mechanics Chalmers University of Technology Goteborg, Sweden*, 30-130.
- [32] Gullberg, P., & Lofdahl, L. (2008). 3D fan modeling strategies for heavy duty vehicle cooling installations – CFD with experimental validation. *FISITA World Automotive*
- [33] Gullberg, P., Löfdahl, L., Adelman, S., and Nilsson, P. (2009). A correction method of stationary fan CFD MRF simulations. *SAE World Congress 2009*, 2009-01-0178
- [34] Gullberg, P., Löfdahl, L., Adelman, S., and Nilsson, P. (2009). An Investigation and correction method of stationary fan CFD MRF simulations. *Vehicle Thermal Management Systems 2009*, 2009-01-3067
- [35] Gullberg P., Löfdahl, L., Nilsson, P., and Adelman, S. (2010). Continued study of the error and consistency of fan CFD MRF models. *SAE World Congress 2010*, 2010-01-0553
- [36] Wang, A., Xiao, Z., & Ghazialam, H. (2005). Evaluation of the Multiple Reference Frame (MRF) model in a truck fan simulation. *SAE Technical Paper Series*. doi:10.4271/2005-01-2067
- [37] Kakaç, S., & Liu, H. (1998). *Heat exchangers: Selection, Rating, and Thermal Design*. Boca Raton, FL: CRC Press.
- [38] Kays, W. M., & London, A. L. (1984). *Compact Heat Exchangers*. New York: McGraw-Hill Book Co.

- [39] Kolditz, O. (2002). *Computational Methods in Environmental Fluid Mechanics*. Berlin: Springer.
- [40] CD-adapco, STAR-CCM+, V9.06, User Manual, 2014.
- [41] Versteeg, H. K., & Malalasekera, W. (2007). *An Introduction to Computational Fluid Dynamics: The Finite Volume Method*. Harlow, England: Pearson Education Ltd.
- [42] Shih, T. (1997). *Modeling of turbulent swirling flows*. Washington, D.C.: National Aeronautics and Space Administration.
- [43] White, F. M. (1986). *Fluid mechanics*. New York: McGraw-Hill.
- [44] Walter, J., (2001) Automotive cooling system component. *Texas Tech University, U.S.*
- [45] Shimizu, T., Abe, T., Sunayama, Y., & Watanabe, S., (2009). Simultaneous evaluation on aerodynamics and air-cooling performances for motorcycle using CFD analysis. *SAE Technical Paper Series*. Paper #: 2009-32-0138
- [46] Biswadip, S., Vinod, K., Ranganath, S. V. K., Gyan, A. (2006) CFD prediction to optimize front end cooling module of a passenger vehicle. *International Refrigeration and Air Conditioning Conference*. Paper 845.
- [47] Huang, K. D., & Tzengz, C. S. (2004). Optimization of size of vehicle and flow domain for underhood airflow simulation. *Journal of Automobile Engineering* , 218 (D9), 945-951. doi:0954-4070
- [48] Williams, J., & Vemaganti, G. (1998). CFD quality - a calibration study for front-end cooling airflow. *SAE Technical Paper Series*. doi:10.4271/980039
- [49] 62.1 user's manual: ANSI/ASHRAE Standard 62.1-2004: ventilation for acceptable indoor air quality. (2005). Atlanta, GA: American Society of Heating, Refrigerating and Air-Conditioning Engineers.

APPENDIX A – STANDARD VELOCITY CORRECTIONS

$$\text{Humidity Ratio } (W) = \frac{(1093 - 0.556T^*) \cdot W^* - 0.25(T - T^*)}{(1093 + 0.444T - T^*)}$$

Where T^* = wet bulb temperature
 T = dry bulb temperature

$$\text{Specific Volume Air } (v_{air}) = 53.352 \cdot \left(\frac{T(^{\circ}R)}{(P_{bar} - \Delta P_{nozzle \ to \ bar}) \frac{lb}{ft^2}} \right) (1 + 1.6078W)$$

$$\text{Density Air } (\rho_{air}) = \frac{1}{v_{air}} (1 + W)$$

$$\text{Nozzle Airflow } (F_{nozzle}) = K_{nozzle} \frac{\sqrt{\delta P_{nozzle}}}{\rho_{air \ nozzle}}$$

Where K_{nozzle} = nozzle coefficient
 δP_{nozzle} = differential pressure across nozzle

$$\text{Mass Airflow } (\dot{m}_{air}) = (F_{nozzle})(\rho_{air \ nozzle})$$

$$\text{Airflow Standard } (F_{std}) = \frac{\dot{m}_{air}}{\rho_{standard}}$$

Where $\rho_{standard}$ = standard air density

-These equations were obtained from [49]

APPENDIX B – TOC AND CONDENSER DATA

Transmission Oil Cooler (TOC) – User-defined look-up tables for heat transfer rate as a function of mass flow rate through the heat exchanger

m (kg/s)	Q (W)
0.01	533.2
0.02	1037
0.03	1511
0.04	1955
0.05	2370
0.06	2755
0.07	3110
0.08	3436
0.09	3732
0.1	3998

Condenser – User-defined look-up tables for heat transfer rate as a function of mass flow rate through the heat exchanger

m (kg/s)	Q (W)
0.1	2230
0.2	4326
0.3	6288
0.4	8117
0.5	9811
0.6	11372
0.7	12800
0.8	14094
0.9	15254
1	16280
1.1	17172
1.2	17931
1.3	18556
1.4	19047
1.5	19405
1.6	19629

Transmission Oil Cooler (TOC) – Geometry and Test Data

TOC Core

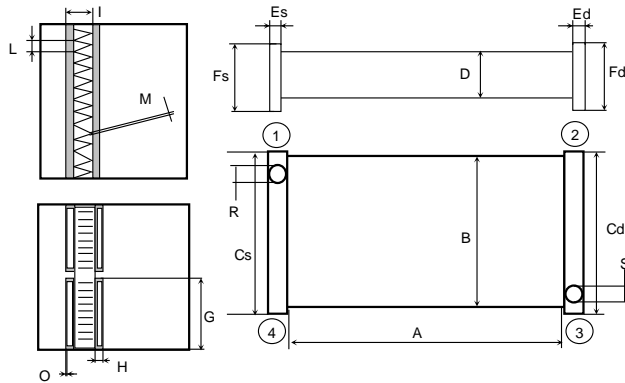
Oil cooler:

Tech *Technology**

A	Oil cooler core length	545.0	mm
B	Oil cooler core height	79.5	mm
D	Oil cooler core thickness	24.0	mm
G	Water tubes length	24.0	mm
H	Water tubes height	3.0	mm
O	Water tubes thickness	0.4	mm
I	Water tubes pitch	7.5	mm
L	Fin pitch	2.50	mm
M	Fin thickness	0.08	mm
R	Top hoses (Right/left) internal diameter	10.3	mm
S	Down hoses (Right/left) internal diameter	10.3	mm

Es	Left tank length	28	mm
Fs	Left tank thickness	28	mm
Cs	Left tank height	117.5	mm
Ed	Right tank length	28	mm
Fd	Right tank thickness	28	mm
Cd	Right tank height	117.5	mm
1	Hoses location: top, left		
2	Hoses location: top, right		
3	Hoses location: down, right		
4	Hoses location: down, left		

28	mm
28	mm
117.5	mm
28	mm
28	mm
117.5	mm



TOC Test Data

Air Side				Tube Side				
[m/s]	[kg/s]	[Pa]	[%]	[kg/s]	[lph]	[kPa]	[kW]	[W/dm ² °C]
1	0.05	22.39	0.735	0.068	300	15.4	2.53	10.31
1	0.05	22.43	0.756	0.095	420	20.31	2.59	10.27
1	0.05	22.45	0.768	0.122	540	25.24	2.63	10.27
1	0.05	22.46	0.775	0.149	660	30.18	2.65	10.25
2	0.1	73.81	0.523	0.068	300	17.06	3.68	21.1
2	0.1	73.84	0.552	0.095	420	22.01	3.87	21.02
2	0.1	73.86	0.568	0.122	540	26.95	3.98	20.99
2	0.1	73.87	0.579	0.149	660	31.89	4.05	20.97
3	0.15	128.4	0.401	0.068	300	18.04	4.3	32.11
3	0.15	128.39	0.431	0.095	420	23.06	4.61	32.03
3	0.15	128.39	0.449	0.122	540	28.03	4.78	31.91
3	0.15	128.39	0.46	0.149	660	32.99	4.9	31.9
4	0.2	193.51	0.331	0.068	300	18.81	4.77	43.24
4	0.2	193.47	0.354	0.095	420	23.77	5.08	43.07
4	0.2	193.43	0.371	0.122	540	28.78	5.32	43.01
4	0.2	193.41	0.382	0.149	660	33.76	5.47	42.9

Condenser – Geometry and Test Data

Condenser Core		
frontal area	27.71	(dm ²)
thickness	16	(mm)
width	620	(mm)
height	447	(mm)
inner path channels	56-13(SC)	
fin pitch	20	(n)
	1.38	(mm)
finned tube width	620	(mm)
finned tube depth	16	(mm)
number of fins	70	(n)
number of tubes	69	(n)
tube periodicity	6.4	(mm)
external tube height	1	(mm)
air side hydraulic diameter	2.2	(mm)
water-side cross sectional area per tube	5.9	(mm ²)
water side hydraulic diameter	0.55	(mm)
collector cross sectional area	150	(mm ²)
fin thickness	0.07	(mm)
fin height	5.4	(mm)
fin length	620	(mm)
water side cooling area to total area	18.8	(%)

Condenser Test Data

MEASURED						SIMULATION					
va (m/s)	m'a (kg/h)	Q' (kW)	Dpa (Pa)	m'refr (kg/h)	Dprefr (bar)	va (m/s)	m'a (kg/h)	Q' (kW)	Dpa (Pa)	m'refr (kg/h)	Dprefr (bar)
1	1107	6.5	6	144.3	0.7	1	1143	7.1	9.2	165	0.69
1.5	1660					1.5	1714	9.8	16.7	228.7	1.09
2	2214	12	12	248.3	1.84	2	2286	12.2	25.3	279.8	1.47
2.5	2767					2.5	2857	14.1	35	322.2	1.84
3	3321	14.9	36.7	320.7	2.56	3	3429	15.7	45.7	357.9	2.19
3.5	3874					3.5	4000	17.1	57	388	2.51
4	4428	15.9	57.4	373.9	3.11	4	4571	18.4	69.2	413.8	2.82
4.5	4981					4.5	5143	19.5	82.1	435.9	3.07
5	5535	18.2	81	413.9	3.52	5	5714	20.4	95.6	455.1	3.31

APPENDIX C – ISOLATED RADIATOR TEST RESULTS

Isolated radiator test – iso-thermal conditions

AIRSIDE DATA						
SI units airside						
		step 1	step 2	step 3	step 4	step 5
Pbar	Pa	97788.41	97770.12	97753.53	97714.58	97648.55
corr delta P air	Pa	33.64864	81.56876	119.599	162.7429	195.7184
Tair sup	°C	43.10718	43.26255	43.19647	43.35735	43.49148
Tair rtn	°C	43.02615	42.93961	42.98917	43.12134	43.07689
DTair	°C	-0.08103	-0.32283	-0.20693	-0.23575	-0.41467
Mair	kg/s	0.663755	1.04553	1.303428	1.570178	1.752454
Fair std	SCFM	1170.66	1844	2298.85	2769.32	3090.8
VEL AIR ST	m/s	1.901205	2.994731	3.733429	4.497497	5.019578
density	kg/m3	1.201001	1.201	1.201001	1.200998	1.201002
velocity at outlet	CALC	0.679654	1.070574	1.334648	1.607791	1.794428

Isolated radiator test – with heat transfer

AIRSIDE DATA		step 1	step 2	step 3	step 4	step 5
Pbar	Pa	97623.51	97595.4	97571.69	97582.87	97513.45
corr delta P air	Pa	36.50408	37.29315	37.65248	37.91675	38.46395
Tair sup	K	316.4939	316.4678	316.5356	316.5961	316.4472
Tair rtn	K	345.0689	349.7667	351.0583	351.6967	352.005
DTair	K	28.575	33.29889	34.52278	35.10056	35.55778
Mair	kg/s	0.658476	0.659674	0.659713	0.658845	0.659377
VEL AIR ST	sFT/M	371.277	371.952	371.974	371.485	371.784
VEL AIR ST	m/s	1.886087	1.889516	1.889628	1.887144	1.888663
COOLANT SIDE DATA						
Tsup cool	K	361.4278	361.1994	361.0489	360.9917	360.935
Tret cool	K	347.6311	353.86	356.1261	357.3461	358.0439
dTcool cal	K	13.79667	7.339444	4.922778	3.645556	2.891111
Pin rad	Pa	86089.32	98634.33	112703.8	127979.1	150944.9
corr dPrad cool	Pa	2241.651	9829.649	22510.63	39886.03	61426.08
Fcool	kg/s	0.327237	0.712932	1.092764	1.477781	1.861392
CAPACITIES						
Qair tot	KW	18.98271	22.16069	22.97636	23.33074	23.65303
Qcool tot	KW	18.84652	21.85554	22.47392	22.51214	22.48702
%dif cool	%	0.719999	1.38739	2.21078	3.5724	5.05455
Qcool avg	KW	18.9146	22.00811	22.72514	22.92144	23.07003

Continued

step 6	step 7	step 8	step 9	step 10	step 11	step 12
97613.01	97622.49	97635.02	97665.83	97768.78	97899.15	97916.43
86.70282	88.31307	89.31664	89.44678	89.53836	127.3546	130.095
316.6144	316.5144	316.5111	316.4828	316.4789	316.7478	316.6217
340.3039	346.4433	348.2511	349.1933	349.7067	337.4867	344.125
23.68944	29.92889	31.74	32.71056	33.22778	20.73889	27.50333
1.044805	1.041939	1.04296	1.041569	1.041244	1.306535	1.304569
589.107	587.488	588.066	587.281	587.099	736.68	735.57
2.992664	2.984439	2.987375	2.983387	2.982463	3.742334	3.736696
361.0139	361.3044	361.08	361.0333	360.9767	360.6433	361.3211
342.8733	350.7583	353.8211	355.5483	356.5883	340.5506	349.0728
18.14056	10.54611	7.258889	5.485	4.388333	20.09278	12.24833
84791.04	97587.71	112062.6	126581.5	150720.1	86507.83	98139.98
2448.225	9553.928	22207.46	39480	61365.14	2565.526	9658.314
0.326487	0.70994	1.089589	1.477176	1.860023	0.326168	0.711085
24.93331	31.41399	33.34709	34.32155	34.85318	27.28193	36.12599
24.7121	31.26424	33.03585	33.84678	34.10322	27.33858	36.36133
0.890982	0.477778	0.937963	1.39325	2.17712	-0.20772	-0.64936
24.82271	31.33897	33.19147	34.08417	34.47805	27.31027	36.24381

Continued

step 13	step 14	step 15	step 16	step 17	step 18	step 19
97926.25	97929.97	98004.81	98129.77	98121.98	98135.18	98191.06
131.2559	131.9681	132.4483	171.4498	175.3409	176.5953	177.1094
316.6544	316.6767	316.6883	316.8439	316.755	316.7911	316.8378
346.2278	347.3111	347.8878	335.3261	342.055	344.3461	345.5494
29.57333	30.63444	31.19944	18.48222	25.3	27.555	28.71167
1.305091	1.304327	1.305484	1.566829	1.565067	1.566784	1.564463
735.865	735.435	736.088	883.446	882.452	883.42	882.112
3.738194	3.73601	3.739327	4.487906	4.482856	4.487774	4.481129
361.11	361.055	360.9622	360.5639	361.315	361.1294	361.0456
352.575	354.5478	355.7117	339.0228	347.735	351.5489	353.7339
8.535	6.507222	5.250556	21.54111	13.58	9.580556	7.311667
113467	128268.7	151787.4	84817.93	98122.74	113287.8	128495.5
22451.67	39720.77	61335.49	2421.142	9590.608	22314.47	39678.16
1.093581	1.479762	1.859759	0.326521	0.709018	1.092523	1.482657
38.86034	40.23104	41.01002	29.14753	39.85532	43.45453	45.21237
38.98109	40.224	40.79754	29.33788	40.19382	43.70774	45.2786
-0.31083	0.017749	0.519734	-0.65113	-0.84613	-0.58082	-0.14652
38.92072	40.22752	40.90364	29.24275	40.02442	43.58113	45.24548

Continued

step 20	step 21	step 22	step 23	step 24	step 25
98201.22	98340.06	98356.31	98363.76	98380.02	98363.09
177.7026	201.0719	198.7072	197.84	197.7347	197.7514
316.8289	317.0089	316.8722	316.9639	316.9822	316.9928
346.1889	334.0489	341.0128	343.4739	344.7506	345.3978
29.36	17.04	24.14056	26.51	27.76833	28.405
1.566353	1.73682	1.700049	1.686872	1.680643	1.677717
883.176	979.291	958.558	951.131	947.619	945.966
4.486534	4.974798	4.869475	4.831745	4.813905	4.805507
360.9722	360.4472	361.1706	361.0672	361.0361	360.8956
355.045	338.1733	347.0494	351.0917	353.3756	354.7033
5.927222	22.27389	14.12111	9.975556	7.660556	6.192222
151091.7	85087.51	98133.77	114207.5	128606.5	151935.6
61345.76	2568.035	9659.142	22211.74	39457.53	61435.53
1.859721	0.326664	0.710473	1.094791	1.47822	1.86059
46.28764	29.78393	41.30251	45.00546	46.96816	47.96079
46.04674	30.34663	41.87693	45.60391	47.29727	48.12491
0.522006	-1.87106	-1.38072	-1.32137	-0.69852	-0.34192
46.16719	30.06528	41.58972	45.30468	47.13257	48.04285

VITA AUCTORIS

Name: Stefan Tojcic

Year of Birth: 1991

Place of Birth: Sarajevo, BIH

Education: University of Windsor
Windsor, ON
B.Sc in Mechanical Engineering, 2014

University of Windsor/Politecnico di Torino
Windsor, ON/Torino, IT
M.A.Sc. International Master's in Automotive Engineering, 2017